# Channelized lava flows at the East Pacific Rise crest 9°–10°N: The importance of off-axis lava transport in developing the architecture of young oceanic crust

**S. A. Soule and D. J. Fornari**
Geology and Geophysics, Woods Hole Oceanographic Institution, Clark South, 272C, MS #24, 286 Woods Hole Road, Woods Hole, Massachusetts 02543, USA (ssoule@whoi.edu)

**M. R. Perfit**
Department of Geological Sciences, University of Florida, Gainesville, Florida 32611, USA

**M. A. Tivey**
Geology and Geophysics, Woods Hole Oceanographic Institution, Clark South, 272C, MS #24, 286 Woods Hole Road, Woods Hole, Massachusetts 02543, USA

**W. I. Ridley**
U.S. Geological Survey, Denver Federal Center, Denver, Colorado 80225, USA

**H. Schouten**
Geology and Geophysics, Woods Hole Oceanographic Institution, Clark South, 272C, MS #24, 286 Woods Hole Road, Woods Hole, Massachusetts 02543, USA

[1] Submarine lava flows are the building blocks of young oceanic crust. Lava erupted at the ridge axis is transported across the ridge crest in a manner dictated by the rheology of the lava, the characteristics of the eruption, and the topography it encounters. The resulting lava flows can vary dramatically in form and consequently in their impact on the physical characteristics of the seafloor and the architecture of the upper 50–500 m of the oceanic crust. We have mapped and measured numerous submarine channelized lava flows at the East Pacific Rise (EPR) crest 9°–10°N that reflect the high-effusion-rate and high-flow-velocity end-member of lava eruption and transport at mid-ocean ridges. Channel systems composed of identifiable segments 50–1000 m in length extend up to 3 km from the axial summit trough (AST) and have widths of 10–50 m and depths of 2–3 m. Samples collected within the channels are N-MORB with Mg# indicating eruption from the AST. We produce detailed maps of lava surface morphology across the channel surface from mosaics of digital images that show lineated or flat sheets at the channel center bounded by brecciated lava at the channel margins. Modeled velocity profiles across the channel surface allow us to determine flux through the channels from 0.4 to $4.7 \times 10^3$ m³/s, and modeled shear rates help explain the surface morphology variation. We suggest that channelized lava flows are a primary mechanism by which lava accumulates in the off-axis region (1–3 km) and produces the layer 2A thickening that is observed at fast and superfast spreading ridges. In addition, the rapid, high-volume-flux eruptions necessary to produce channelized flows may act as an indicator of the local magma budget along the EPR. We find that high concentrations of channelized lava flows correlate with local, across-axis ridge morphology indicative of an elevated magma budget. Additionally, in locations where channelized flows are located dominantly to the east or west of the AST, the ridge crest is asymmetric, and layer 2A appears to thicken over a greater distance from the AST toward the side of the ridge crest where the channels are located.

**Components:** 14,922 words, 22 figures, 5 tables.

**Keywords:** channels; lava; lava morphology; ridge-crest; submarine.

## 1. Introduction

[2] At fast spreading mid-ocean ridges (MORs), the upper portion of the oceanic crust is composed of a 50–500 m thick layer of extrusive volcanics [e.g., *Christeson et al.*, 1992]. Many tens to hundreds of lava flows erupting from the axial summit trough (AST) and at off-axis (2–5 km) eruptive vents and fissures overlap and interfinger to build up this layer [e.g., *Perfit et al.*, 1994; *Perfit and Chadwick*, 1998; *Fornari et al.*, 2004]. Over the past twenty years we have gained insight into the physical characteristics (e.g., density, porosity, thickness) of the extrusive volcanic layer (layer 2A) through in situ geophysical experiments [*Christenson et al.*, 1992, 1994a, 1994b, 1996; *Detrick et al.*, 1993; *Harding et al.*, 1993; *Vera and Diebold*, 1994; *Kent et al.*, 1994; *Carbotte et al.*, 1997]. The geophysical data integrate over the thickness of this layer revealing average crustal properties. However, fundamental questions remain regarding the details of how this layer is constructed. Understanding the intricacies of this process such as the timescale and rates of individual eruptions, the volume and length of individual flows, and the recurrence interval of eruptive activity would provide insight into the construction of this geologically important layer as well as how the crustal architecture influences shallow hydrothermal pathways [e.g., *Delaney et al.*, 1998; *Fornari et al.*, 1998, 2004; *Bach et al.*, 2004] and habitat for subsurface microorganisms [e.g., *Edwards et al.*, 2003].

[3] *Delaney et al.* [1998] describe MOR dike emplacement as the irreducible, quantum event of upper oceanic crustal accretion. While this may be true for Layer 2B in a two-dimensional, ridge-perpendicular sense, the same cannot be said for the development of layer 2A, which grows vertically and laterally, thickening 2–3 times within 1–4 km of the AST [e.g., *Harding et al.*, 1993; *Christeson et al.*, 1994a, 1994b, 1996; *Sohn et al.*, 2004]. In this case, accretion occurs through the eruption of individual lava flows that, while erupted at the ridge axis, can broadly distribute lava across the ridge crest. Thus, for layer 2A accretion at the EPR, the emplacement of an individual lava flow could be considered a quantum event, or building block of the upper oceanic crust.

[4] Reliably resolving individual lava flows requires remotely sensed data of higher resolution than has been possible in the past due to flow dimensions, e.g., widths on the order of tens to hundreds of meters, thicknesses of <10 m, and lengths of hundreds of meters to kilometers [e.g., *Scheirer et al.*, 2000]. In this study we utilize new instrumentation including the DSL120A that produces side-scan sonar data at 2 m per pixel when collecting at 100 m altitude and the Imagenex scanning altimeter that produces bathymetry at 5 m per pixel when collecting at 40 m altitude to 0.5 m per pixel when collecting at 5 m altitude. These data are collected over length scales of kilometers (Imagenex) to tens of kilometers (DSL120A) necessary to capture numerous individual lava flows across the diverse geophysical, hydrothermal, and biological provinces that exist on fast spreading MORs. Data from these high-resolution sonars, as well as still and video seafloor imagery and in situ observation and sampling, were collected along a 58-km-long section of MOR during two cruises (AT7-4 and AT11-7) to the EPR at 9°–10°N (Figure 1). We integrate these data sets with geochemical analyses of recovered samples and numerical modeling to provide the first comprehensive description of submarine channelized lava flows, which have only recently been recognized on fast and superfast spreading ridges where high-resolution data sets have been collected [*Ryan et al.*, 1999; *Sakimoto and Gregg*, 2001; *Sinton et al.*, 2002; *Cormier et al.*, 2003, W. B. Garry et al., Formation of submarine lava channel textures: Insights from laboratory simulations, submitted to *Journal of Geophysical Research*, 2005 (hereinafter referred to as Garry et al., submitted manuscript, 2005)].
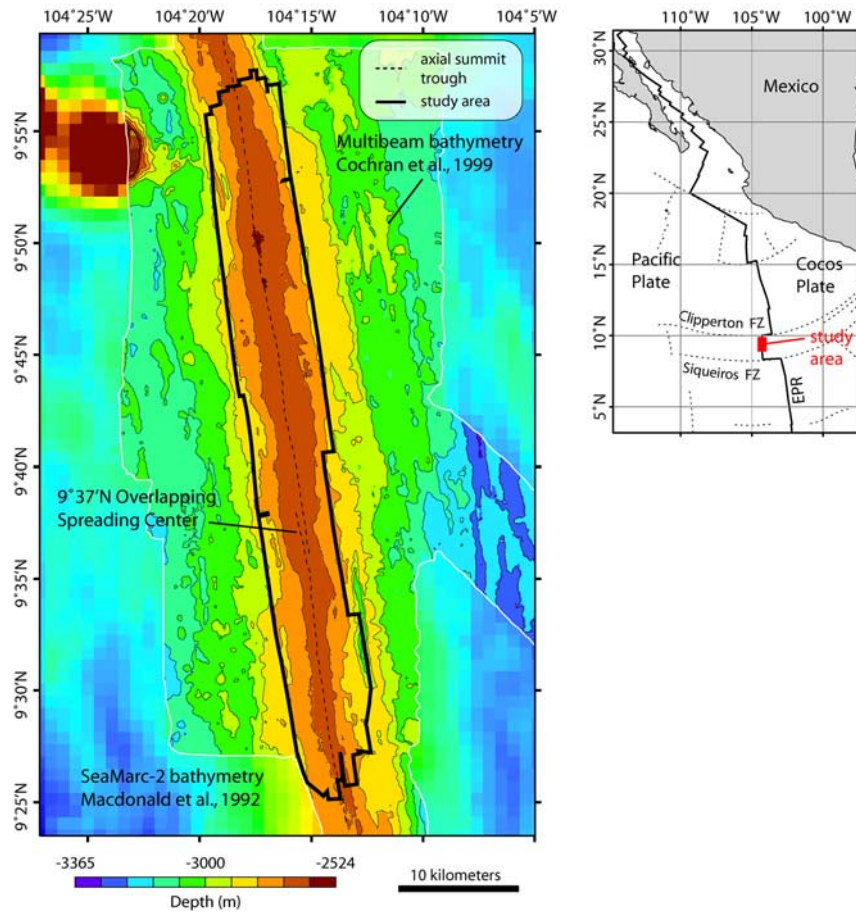
**Figure 1.** Location of study area between 9°25′N and 10°N at the East Pacific Rise (EPR) between the Clipperton and Siqueiros fracture zones. The study area, outlined in black, marks the location of DSL-120A side-scan sonar data and is 58 km long and ~8 km wide. It is centered on the axial summit trough (AST), and the overlapping spreading center at 9°37′N is marked. The contour interval is ~84 m.

[5] Channelized flows are believed to represent the high-effusion-rate and high-flow-velocity end-member of submarine eruptions [*Gregg and Fink*, 1995; *Sakimoto and Gregg*, 2001; Garry et al., submitted manuscript, 2005]. We believe they are important in transporting lava up to 3 km away from their eruption site at the AST, thereby providing a viable mechanism to explain the development and rapid off-axis thickening of the upper oceanic crust. Below we describe the physical properties of EPR lava channels, including their width, depth, and surface morphologies, and utilize these properties to model their emplacement and place constraints on the velocity and volumetric flux of their emplacement. Observations and detailed sampling of these flows with the submersible *Alvin* and subsequent geochemical analysis allow us to quantify field relations that may be unclear in remotely sensed data. We show that lava channels form during high effusion rate eruptions centered

at the AST and efficiently transport lava at rates of $10^3$ m³/s over distances of 1−3 km. Finally, we document lava channel distribution over a 58 km long section of the EPR and relate that distribution to broad-scale properties of the ridge crest and by inference crustal accretion processes within the volcanic extrusive layer at fast spreading MORs.

## 1.1. East Pacific Rise Geology

[6] The first-order segment of the EPR between the Siqueiros and Clipperton transforms (8−11°N) is spreading at a full rate of 11 cm/yr [*Carbotte and Macdonald*, 1992]. Within this region are two second-order segments separated by an overlapping spreading centers at 9°03′N [e.g., *Carbotte and Macdonald*, 1992; *Macdonald et al.*, 1992] and 9°37′N [e.g., *Smith et al.*, 2001] and many third- and fourth-order segments detected by multibeam

bathymetry and near-bottom investigations [*Haymon et al.*, 1991; *Macdonald et al.*, 1984; *Langmuir et al.*, 1986; *Batiza and Margolis*, 1986; *Scheirer and Macdonald*, 1993; *White et al.*, 2002]. The ridge axis between ~9°30′N and 9°50′N is characterized by a broad summit plateau that contains a narrow (~40–300 m wide) depression, the AST, where nearly all of the hydrothermal venting and volcanic eruptions are focused [*Haymon et al.*, 1991; *Fornari et al.*, 1998, 2004; *Schouten et al.*, 2002]. A ~4 km wide region of bright acoustic backscatter centered on the AST delineates the neo-volcanic zone, a band of recently emplaced volcanics [*Schouten et al.*, 2002; *White et al.*, 2002; *Fornari et al.*, 2004]. Along axis, the neovolcanic zone narrows and widens in response to differences in the volcanic history of a particular area. Pillow mounds 5–20 m in height are formed by off-axis eruptions at the margins and outside of the neovolcanic zone [*Perfit et al.*, 1994] and at segment ends [*White et al.*, 2002]. The neovolcanic zone is nearly free of faults and fissures, suggesting that the rate of tectonic deformation is outpaced by the rate of volcanic repaving of the seafloor. At ~2–4 km off-axis, faults and fissures are commonly observed in side-scan sonar data that stem further off-axis advance of lava. Within the neovolcanic zone, slopes are shallow (0–5°), but can increase (5–10°) farther off-axis.

[7] The neovolcanic zone at this section of the EPR is acoustically heterogeneous reflecting the diversity of volcanic emplacement styles along the ridge axis [*Fornari et al.*, 1998; *Kurras et al.*, 2000; *Schouten et al.*, 2002]. Acoustic backscatter intensity (gray scale) is primarily a measure of the surface roughness of the seabed. In seafloor lava flows, roughness is strongly influenced by the style of eruption and resulting surface morphology of the lava [e.g., *Griffiths and Fink*, 1992]. Even from the first observations of MOR volcanics (FAMOUS; *Bellaiche et al.* [1974]; *Ballard et al.* [1975]; *Ballard and Van Andel* [1977]), researchers recognized distinct surface morphologies on submarine flows. All flows can broadly be classified as either pillow, lobate, or sheet lava (see *Perfit and Chadwick* [1998] for a review), but as with subaerial lava flows, a spectrum of morphologies exists between each end-member [e.g., *Soule et al.*, 2004].

[8] Our understanding of submarine lava flow behavior is limited by the scarcity of observations of active eruptions. In one case, a seafloor instrument was trapped in the crust of an actively advancing flow at the Juan de Fuca Ridge (JdFR) [*Fox et al.*, 2001]. In addition, submersible dives have been conducted on recently emplaced, still-cooling lava flows at the EPR [*Haymon et al.*, 1993] and the CoAxial segment of the JdFR [*Embley et al.*, 2000]. In the absence of observations of active submarine lava flows, lava flow surface morphology can serve as a primary indicator of emplacement dynamics. Our understanding of the formation of submarine lava surface morphology comes in part from analog modeling using polyethylene glycol (PEG) wax [*Fink and Griffiths*, 1990, 1992; *Griffiths and Fink*, 1992; *Gregg and Fink*, 1995]. These experiments parameterize surface morphology formation as a balance between the timescale of cooling, which is a proxy for the rate of crust formation, and timescale of advection, which is a proxy for the rate of crust disruption. It should be noted that in subaerial lava flows an additional parameter, effective viscosity, must be considered due to cooling and crystallization during flow [*Cashman et al.*, 1999; *Soule et al.*, 2004]. In submarine lava flows, however, there is no evidence of extensive cooling and resultant crystallization of the flow interior during emplacement [e.g., *Adams*, 2001], ensuring that the lava remains an iso-viscous Newtonian fluid, and that the conceptual framework of the PEG experiments can be applied. Thus it is broadly accepted that individual pillows form at low-volume flux allowing a carapace of quenched lava to stem their advance and limit coalescence between adjacent pillows. Lobate lava is able to spread and coalesce to a greater degree than pillows before a carapace of solidified lava forms. Sheet lava flows form at high flux and crust is unable to form on a timescale to inhibit the lava spreading out as a sheet [e.g., *Perfit and Chadwick*, 1998]. As a result of these emplacement styles, each morphology: pillow, lobate, and sheet, shows lessening surface roughness that aids in their identification in side-scan sonar imagery.

## 2. Lava Channel Properties

[9] Submarine lava channels are distinguished from surrounding lava flows by their low reflectivity (i.e., low sonar backscatter intensity) and depressed local topography (Figure 2). Both properties are strong indicators of the style of eruption that leads to their development. The low reflectivity indicates surface roughness less than the sonar wavelength of 1–10 cm [*Scheirer et al.*, 2000]. As mentioned above, decreasing surface roughness is correlated with increasing flux rates, thus channels
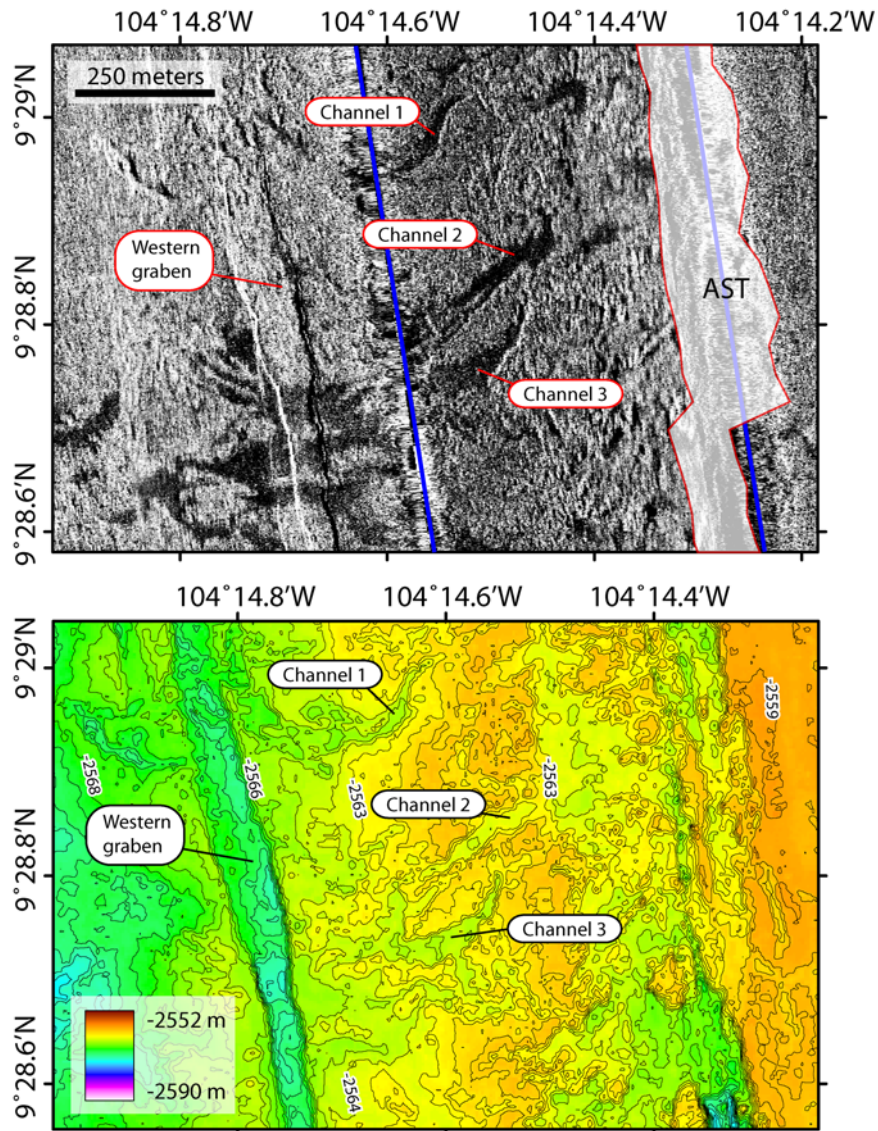
**Figure 2.** Example of acoustic backscatter intensity from (top) DSL-120A side-scan sonar and (bottom) microbathymetry from ABE showing lava channels at 9°28′N. Channels are floored with smooth sheets, resulting in the low-reflectivity, dark streaks visible in the acoustic backscatter image. Channels are drained of lava, resulting in shallow depressions visible in the microbathymetry. Contour intervals are 1 m. Blue lines mark nadirs of sonar swaths. Extent of axial summit trough (AST) is shown in red (D. J. Fornari et al., The axial summit trough and crest of the East Pacific Rise—9°09′–59′N: New insights on submarine eruption and transport processes based on DSL-120A sidescan and ABE sonar surveys, manuscript in preparation, 2005 (hereinafter referred to as Fornari et al., manuscript in preparation, 2005)).

appear to reflect rapid lava extrusion and flow. Their uniformly depressed topography results from a wholesale sagging of the crust as the liquid lava is drained. This sagging is in contrast to the localized collapse observed in lobate flows [e.g., *Engels et al.*, 2003]. For channelized flows, it appears that flux is rapid enough that the flows cannot develop the internal structure (lobe boundaries and lava pillars) [*Gregg and Chadwick*, 1996; *Gregg et al.*, 2000; *Chadwick*, 2003] to support the overlying crust until brittle, local collapse can occur.

[10] Channels are a thermally and mechanically efficient means of transporting lava. There is no consensus on the mechanism by which channels form. Channels may form within a sheet or lobate flow due to flow focusing either by cooling from the edges, thermally induced instabilities in flow velocity, or mechanical instabilities
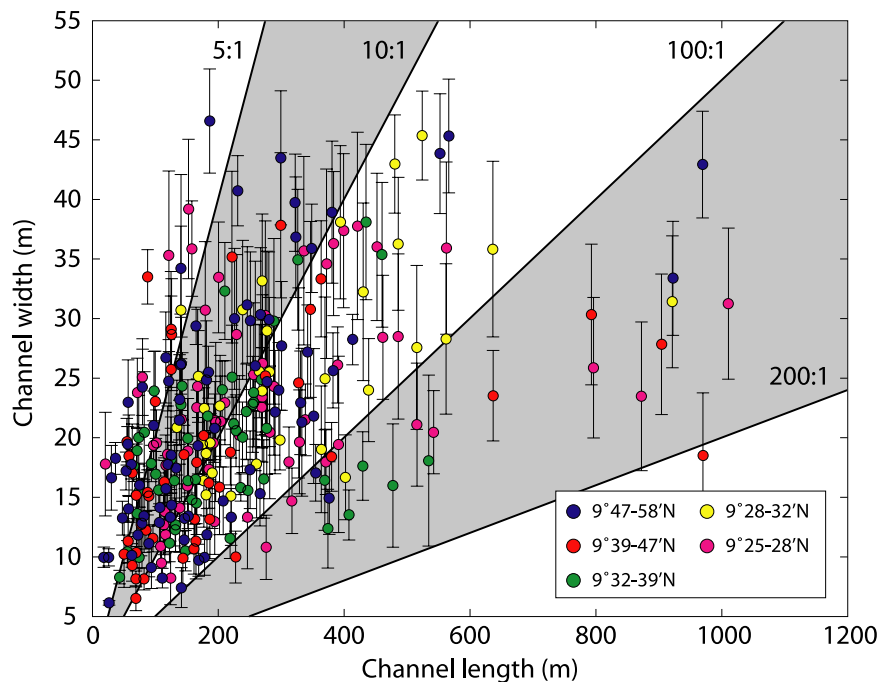
**Figure 3.** Plot showing length and width of channel segments. Colored symbols indicate mean channel width and length from different, along-axis portions of the ridge. Error bars show 1 sigma for channel widths measured every 2 m along individual channel segments. Solid lines indicate the aspect ratios of the channels, which vary from 5:1 to 200:1 and have mean aspect ratio of ~15:1.

in flow velocity arising from interaction with pre-existing topography or solidified lava at the flow front. In addition, lava may advance in a channel directly from the eruptive vent by occupying pre-existing channels or other seafloor features that topographically focus flow. The observations described in this paper do not rule out any of these mechanisms for channel formation, and it is likely that each of them may be appropriate in different settings.

[11] Channels generally occur within a ~2–3 km wide zone to either side of the AST. Channel segments vary in length from 50–1000 m with a mean length of 250 m. Channel widths, determined by measuring widths every two meters along individual segments, can be highly variable (10–50 m) along a single channel segment, with a mean width of 25 m. Channel aspect ratios (length:width) vary from 5 to >100, with a mean aspect ratio of ~15 (Figure 3). Channel paths are sinuous and generally following the steepest local gradient. In many cases pre-existing lava flow fronts and channels determine that path. Channel tortuosity, a measure of path length versus the direct path between the channel ends, ranges from 1–1.6 and shows no correlation to total channel length. In general, underlying slope increased from 0° adjacent to the AST up to 5° 3 km from the AST. We

observe no correlation between the physical characteristics of the channel segments described above and the slope on which they formed.

[12] Highly accurate channel widths and depths were determined on approximately 10 individual flows from high-resolution microbathymetry maps compiled using a 675 kHz Imagenex scanning altimeter and precision pressure and depth sensors mounted on the hull of *Alvin* [*Fornari et al.*, 2004; *Ferrini et al.*, 2004] (Figure 4). The maps cover small areas (typically 10 m × 10 m), but contain dense enough data coverage to be gridded at 0.5 m and resolve depth differences on the order of less than 10 cm. Width was measured as the distance between the uncollapsed margins of the channel, which correlate with distinct transitions in flow surface morphology, and range from 10–50 m. Depth was measured from the level of the deflated roof to the level of the surrounding undeflated lava and ranges from 1.9–3.0 m. We observed no local collapse within the deflated portion of the channels studied; thus we are unable to determine whether the channel has drained entirely (i.e., to the channel floor), and thus channel depth should be considered a minimum. The narrow widths and shallow depths of submarine channels underscore the need for high-resolution data at other MORs in order to resolve these features.
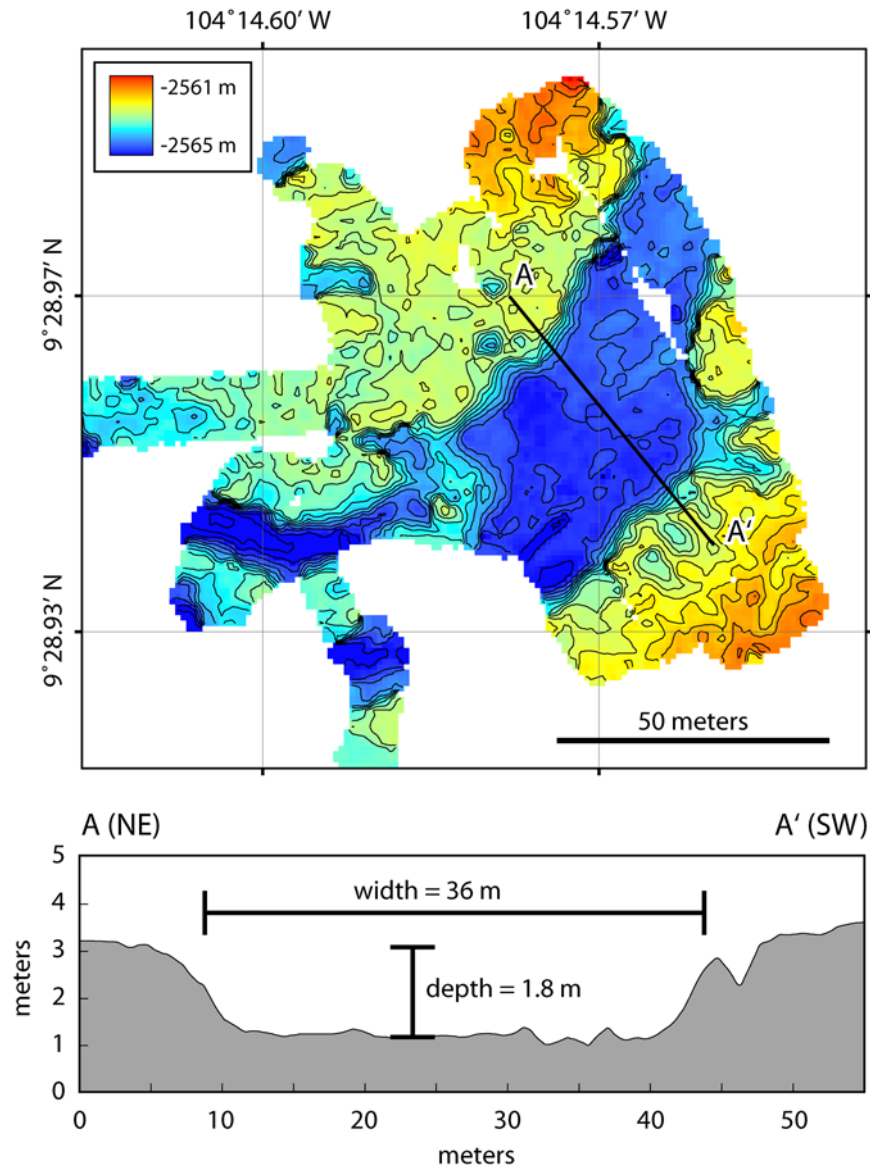
**Figure 4.** (top) Very high-resolution bathymetry collected by an Imagenex 675 kHz scanning altimeter and pressure depth sensors mounted on *Alvin*, contoured at 25 cm depth intervals. A bathymetric transect across the channel shows the nearly rectangular cross section and the methods by which channel depth and width are determined. This channel is part of the Northern channel system at 9°28′N and is shown in mosaics K, L, and M (Figure 8).

[13] We have mapped over 300 channel segments on the basis of the described acoustic and bathymetric characteristics and ground-truthed that mapping with digital seafloor photography (Figure 5). We often observed closely spaced channel segments (less than 10 m apart) aligned end-to-end that when taken as a whole represent a single channel system. However, it was difficult to determine for each channel whether missing channel segments reflect poor preservation (e.g., covered by later lava flows), poor data coverage (e.g., beneath the nadir of the sonar swath), or a portion of the flow that did not develop a channel (e.g., a

lava tube or surface flow developed instead). As a result, determinations of channel properties such as length were made on individual channel segments except where the connection between multiple segments were separated by less than 5 m and were clearly obscured by a non-geological feature (e.g., side-scan nadir).

## 3. Geochemistry

[14] We collected lava samples in and around channels at several EPR study sites for post-cruise
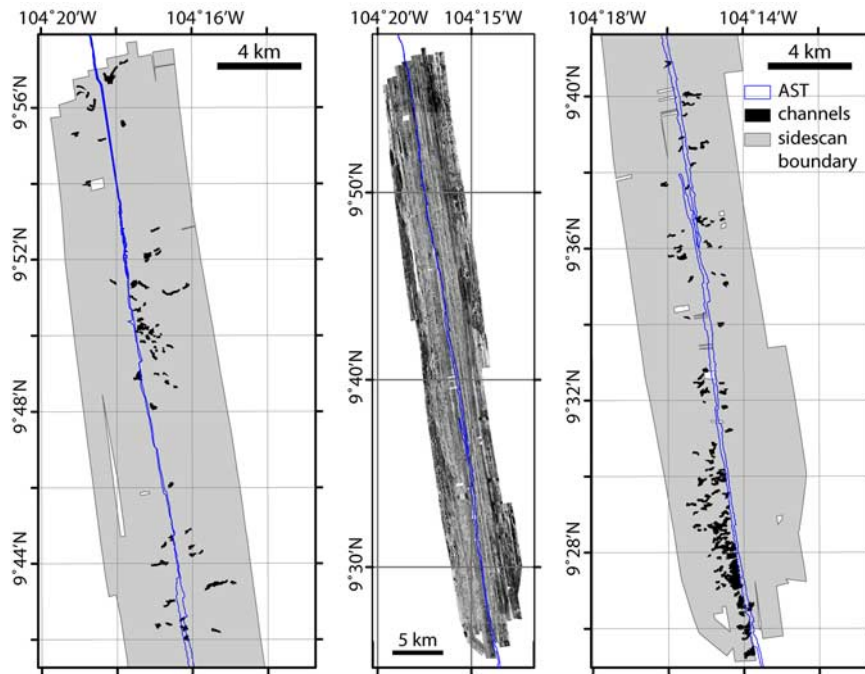
**Figure 5.** Side-scan sonar map of the 9°25′N to 10°N study area on the EPR (center, from Fornari et al., manuscript in preparation, 2005). Channel boundaries along this section of the EPR are shown in black in larger-scale maps at left and right. The boundary of the side-scan sonar data [*Schouten et al.*, 2002] is shown in gray, and the AST boundary is shown in red (Fornari et al., manuscript in preparation, 2005).

analysis using an electron microprobe to aid in identifying individual flows and to address questions regarding the origin of channelized flows, relationships to surrounding lava flows, and physical properties of the lava. Samples of lava with quenched crusts were collected using *Alvin* along channelized flows at 9°29′N and 9°50′N (Figure 6, Table 1). At each sampling site, lava crusts from within the channel, at the channel margin, and outside of the channel were collected.
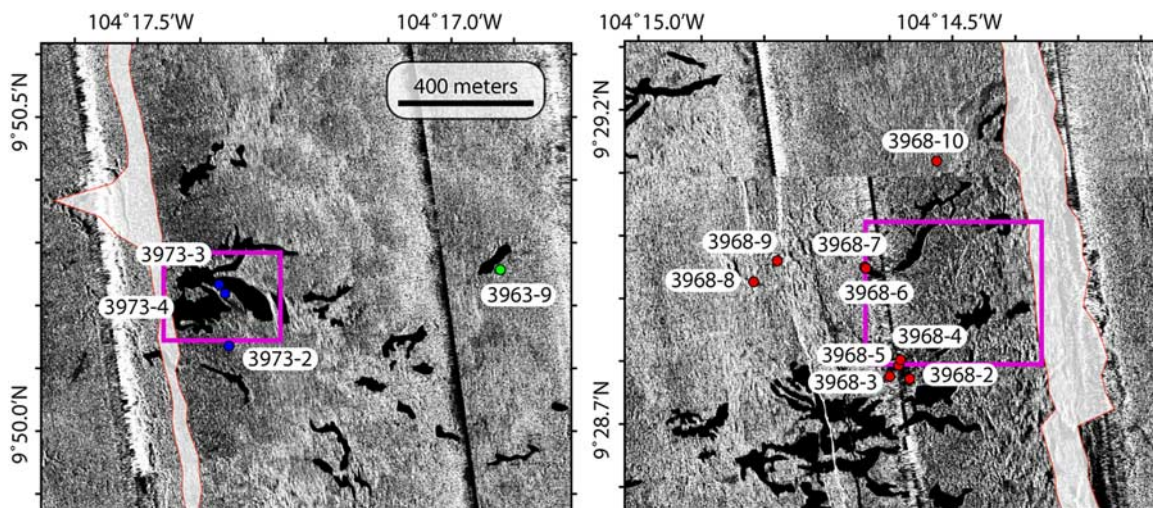


**Figure 6.** Side-scan sonar maps in locations of dedicated *Alvin* dives carried out in 2004 that surveyed lava channels show channels (black) and locations of samples. Samples are named by *Alvin* dive, and sequence of collection during the dive. The AST is shown in white in each map. Red boxes indicate the locations of maps shown in Figure 8. Note that the side-scan sonar map for the 9°28′N area (right) is made from two sonar swaths, hence the offset in the imagery near 9°29.1′N.

**Table 1.**  Sample Location and Description

| Sample | Depth, m | Latitude, °N | Longitude, °W | Dist. From Axis, m | Morphology | Within Channel |
|--------|----------|--------------|----------------|---------------------|------------|----------------|
| *9°50′N Channel System* | | | | | | |
| 3963-9 | 2524 | 9°50.3′ | 104°16.8′ | 1287 | lobate | no |
| 3973-2 | 2507 | 9°50.1′ | 104°17.4′ | 203 | lobate | no |
| 3973-3 | 2509 | 9°50.2′ | 104°17.4′ | 172 | lobate | no |
| 3973-4 | 2509 | 9°50.2′ | 104°17.4′ | 198 | sheet | yes |
| *9°28′N Southern Channel System* | | | | | | |
| 3968-2 | 2564 | 9°28.8′ | 104°14.6′ | 377 | lobate | no |
| 3968-3 | 2566 | 9°28.8′ | 104°14.6′ | 435 | sheet (fold) | yes |
| 3968-4fn,fp | 2566 | 9°28.8′ | 104°14.6′ | 437 | sheet (fold) | yes |
| 3968-4h | 2566 | 9°28.8′ | 104°14.6′ | 437 | brecciated | yes |
| 3968-5 | 2566 | 9°28.8′ | 104°14.6′ | 437 | brecciated | yes |
| *9°28′N Northern Channel System* | | | | | | |
| 3968-6 | 2567 | 9°28.9′ | 104°14.6′ | 606 | sheet (fold) | yes |
| 3968-7 | 2667 | 9°28.9′ | 104°14.6′ | 606 | lobate | no |
| 3968-9 | 3570 | 9°28.9′ | 104°14.6′ | 883 | sheet (fold) | yes |
| 3968-10 | 2565 | 9°29.1′ | 104°14.5′ | 241 | sheet | yes |

[15] Lava crusts from lobate flows contain a glassy layer at their upper surface that varies in thickness from 2 mm to 2 cm (Figure 7a). In most samples, the glassy layer is nearly aphyric (≪1 vol.% crystals) containing rare plagioclase, pyroxene, and olivine microlites. The glassy layer grades into a variolitic layer of radial, feathery plagioclase and skeletal, bladed pyroxenes intergrown with Fe-Ti oxides suggesting slightly less rapid quenching than the upper glassy layer. Varioles gradually coarsen toward the wholly crystalline interior of the crust. At the base of the crust there is another glassy layer, 1–5 mm thick. The lower glassy layer has greater crystal content than the upper glassy layer (up to 25 vol.%) that is composed primarily of clots of plagioclase microphenocrysts. One sample (3973-3), of pillows found at the front of a lobate flow, has the same mineral phases in its upper glassy layer as those found in lobate samples, but in slightly greater concentrations of ~5 vol.%. In all samples, we analyzed the upper glassy layer for major-element abundances as this glass best preserves the composition of the liquid lava at the time of emplacement.
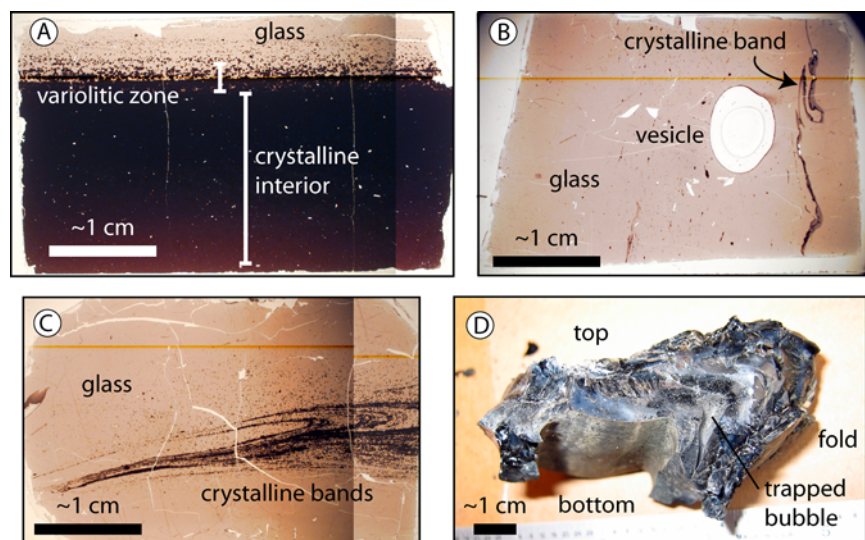


**Figure 7.**  Photomicrographs of thin sections from samples of lobate lava adjacent to a channel (3968-2, Figure 7a), and samples of folded lava from within the channel (3968-4fp, Figure 7b) and (3968-9, Figure 7c). A folded, glassy portion of sample 3968-9 is shown in Figure 7d. Lobate lavas grade from aphyric glass into a variolitic zone of quenched crystals followed by a crystalline interior. These channel samples show tortuous bands of quench crystals and a large vesicle believed to reflect the incorporation of seawater into the flow [e.g., *Perfit et al.*, 2003].

**Table 2.** Averaged Major Element Microprobe Analyses[a]

| Sample | N | $SiO_2$ | $TiO_2$ | $Al_2O_3$ | FeO* | MnO | MgO | CaO | $Na_2O$ | $K_2O$ | $P_2O_5$ | Total | Mg# | $K_2O/TiO_2$ |
|---|---|---|---|---|---|---|---|---|---|---|---|---|---|---|
| | | | | | | | *9°50′N Channel System* | | | | | | | |
| 3963-9 | 23 | 49.87 | 1.14 | 15.98 | 8.98 | 0.17 | 8.85 | 12.31 | 2.55 | 0.09 | 0.09 | 100.04 | 0.661 | 0.077 |
| 3973-2a | 19 | 49.79 | 1.22 | 15.87 | 8.90 | 0.17 | 8.67 | 12.27 | 2.53 | 0.09 | 0.11 | 99.63 | 0.659 | 0.071 |
| 3973-3 | 29 | 50.04 | 1.26 | 15.65 | 9.18 | 0.17 | 8.67 | 12.19 | 2.51 | 0.11 | 0.12 | 99.90 | 0.651 | 0.086 |
| 3973-4 | 30 | 50.29 | 1.20 | 15.82 | 8.86 | 0.17 | 8.69 | 12.17 | 2.53 | 0.10 | 0.11 | 99.95 | 0.660 | 0.087 |
| | | | | | | | *9°28′N Southern Channel System* | | | | | | | |
| 3968-2 | 22 | 50.51 | 1.70 | 14.33 | 10.58 | 0.21 | 7.58 | 11.70 | 2.77 | 0.11 | 0.14 | 99.65 | 0.587 | 0.065 |
| 3968-3 | 24 | 50.93 | 1.70 | 14.24 | 10.61 | 0.20 | 7.64 | 11.64 | 2.80 | 0.13 | 0.17 | 100.08 | 0.588 | 0.079 |
| 3968-4fn | 37 | 51.09 | 1.70 | 14.27 | 10.63 | 0.20 | 7.51 | 11.61 | 2.70 | 0.13 | 0.16 | 100.02 | 0.583 | 0.078 |
| 3968-4fp | 30 | 50.61 | 1.69 | 14.20 | 10.59 | 0.19 | 7.62 | 11.55 | 2.75 | 0.13 | 0.15 | 99.51 | 0.588 | 0.079 |
| 3968-4h | 33 | 50.64 | 1.72 | 14.33 | 10.67 | 0.19 | 7.68 | 11.69 | 2.86 | 0.13 | 0.15 | 100.08 | 0.588 | 0.078 |
| 3968-5 | 12 | 50.57 | 1.66 | 14.29 | 10.57 | 0.20 | 7.73 | 11.57 | 2.74 | 0.11 | 0.15 | 99.61 | 0.591 | 0.066 |
| | | | | | | | *9°28′N Northern Channel System* | | | | | | | |
| 3968-6 | 33 | 50.66 | 1.68 | 14.19 | 10.67 | 0.20 | 7.55 | 11.61 | 2.74 | 0.11 | 0.16 | 99.60 | 0.583 | 0.066 |
| 3968-7 | 12 | 50.72 | 1.66 | 14.28 | 10.57 | 0.20 | 7.71 | 11.62 | 2.68 | 0.11 | 0.15 | 99.74 | 0.591 | 0.068 |
| 3968-9 | 29 | 50.87 | 1.69 | 14.27 | 10.56 | 0.19 | 7.62 | 11.69 | 2.80 | 0.13 | 0.17 | 100.01 | 0.588 | 0.078 |
| 3968-10 | 20 | 50.65 | 1.65 | 14.26 | 10.49 | 0.20 | 7.76 | 11.59 | 2.72 | 0.11 | 0.15 | 99.60 | 0.594 | 0.067 |
| ±2σ | | 0.08 | 0.02 | 0.08 | 0.05 | 0.01 | 0.05 | 0.06 | 0.04 | 0.003 | 0.01 | | | |

[a] Sample indicates *Alvin* dive number followed by station number and sample identifier. N indicates number of analyses on sample; analyses are reported in wt%. FeO* is total Fe. Mg# is atomic $Mg/(Mg + Fe^{2+})$ assuming 90% of Fe is FeO.

[16] Samples of lava crust from within each channel are generally from folds that produce lineations along the channel surface. These folds contain more glass than the lobate lava flows, and the chaotic nature of their formation often makes it difficult to infer what is the upper and lower surface. The interiors of the folds often contain crystal rich bands that vary in thickness from millimeters to centimeters. The tortuous character of some of these bands, relative to those found in lobate lava flows, give a sense of the dynamic nature of the emplacement of lava within the channel (Figures 7b and 7c). The folds often contain large vesicles (>0.5 cm in diameter) that reflect trapped seawater incorporated into the lava as it folded over on itself.

[17] Major element compositions of the samples were analyzed on a JEOL JXA-8800L electron probe microanalyzer at 15 KV and 20 nA current at the USGS microbeam facility in Denver. Up to five zones were analyzed on each sample and ~5 analyses (with a 10 micron beam diameter) were made at each zone. Data was reduced using a full ZAF correction and basalt glasses JDF-D2 and 2392-9 were used as secondary glass "standards" to calibrate microprobe analyses and ensure that data collected over a period of days are compatible and directly comparable to our previous analyses of EPR samples (Table 2) (see *Perfit et al.* [1994], *Perfit and Chadwick* [1998] and *Smith et al.* [2001]

for details of analytical techniques). All analyzed samples have N-MORB compositions, and fall within the compositional range of the entire EPR data set (M. R. Perfit et al., Geochemical variability and petrogenesis of MORB from the East Pacific Rise 9°17′–10°N: Integrating a high resolution geochemical dataset with geological and geophysical observations, manuscript in preparation, 2005 (hereinafter referred to as Perfit et al., manuscript in preparation, 2005)). The Mg# (Mg/Mg + Fe, where Fe = 0.9 Fe total) is distinct between samples from the 9°28′ (~0.59) and 9°50′N (~0.66) areas, and agrees with *Smith et al.*'s [2001] description of along-axis compositional variations.

## 4. Channel Mosaics

[18] We constructed a number of photo mosaics across channels that allowed us to make detailed maps of the lava surface morphologies present on the channel surface. Mosaics were constructed from consecutive digital video and still images taken from *Alvin* using publicly available mosaicking software [*Mayer et al.*, 2004]. Mosaics are composed of a strip of up to 36 still images or 350 video-frames and cover a 2–6 m swath wide over channels 10–40 m across. Individual images are of sufficient resolution to easily identify cracks in the crust that are <3 cm across. Relative position
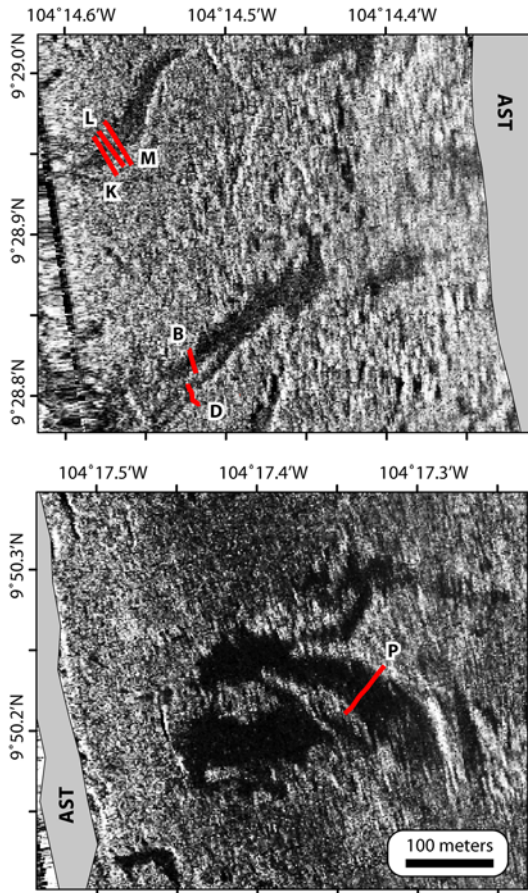
**Figure 8.** Side-scan sonar maps showing the locations of channel crossings (red) where mosaics are constructed. Maps are zoomed-in portions of maps shown in Figure 6.

errors are accumulated as the mosaic is constructed, but in all cases are <1% of the total width of the mosaic. Locations of mosaics are shown in Figure 8 and mosaics and related surface morphology maps are shown in Figures 9–14. Table 3 lists surface morphology properties from two channel systems at 9°28′N and one at 9°50′N.

[19] A characteristic distribution of surface morphologies is apparent across each of the channels we have examined (Figures 9–14). Channels are bound at both margins by lobate lava that shows various degrees of localized collapse. From the outer edge toward the center of each channel examined a brecciated region of varying width is encountered that accommodates the relief created by sagging of the channel roof. The brecciated region is composed of jumbled or hackly textured lava with broken fragments on the order of 10–100 cm across. Individual fragments may contain folds and lineations on their upper surfaces that are common on the flat sheets within the central portion of the channel.

*Perfit and Chadwick* [1998] describe the formation of jumbled and hackly lava as resulting from continued deformation of solidified lava crust accompanying changes in lava viscosity, rate of shear, or eruption rate. Here we use the term brecciated region to describe the marginal zone containing jumbled and hackly fragmental lava.

[20] The brecciated regions vary in their width relative to total channel width. The normalized widths show a bimodal distribution with wide brecciated zones on the southern channel system at 9°28′N and narrow brecciated zones on the northern channel system at 9°28′N. At 9°50′N, no brecciated regions are visible, however, it appears that the channel margins may have been covered by subsequent lava flows that may represent the waning stages of the same eruptive event. At both 9°50′N and 9°28′N, the central part of the channels we mapped contain smooth sheet lava. The central flat sheets always contain flow-parallel lineations, but the density of those lineations is variable, and some channels contain lineations transverse to the flow direction. In the southern channel system at 9°28′N we observed nearly featureless sheets at the channel center, whereas in the northern channel system at 9°28′N and at 9°50′N, the central sheets are densely lineated. These, sometimes subtle, differences in surface morphology across the channels suggest that there may be intrinsic differences
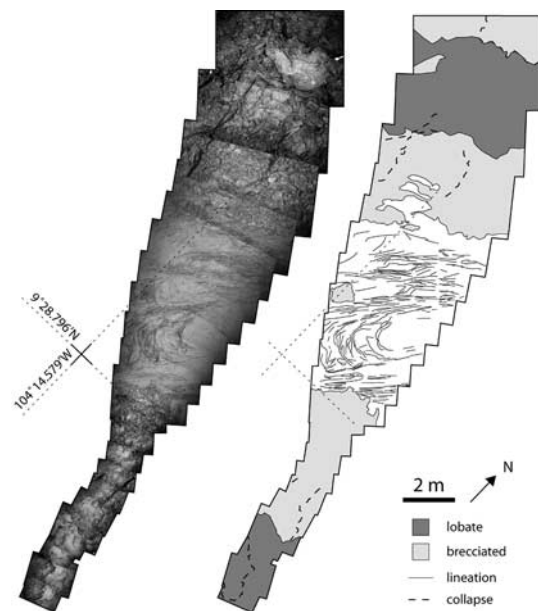


**Figure 9.** (left) Mosaic of digital still images from a downlooking camera mounted on *Alvin* and (right) interpretation of the mosaic. This transect, B, is from the southern channel system at 9°28′N and shows wide brecciated margins and a heavily lineated central sheet.
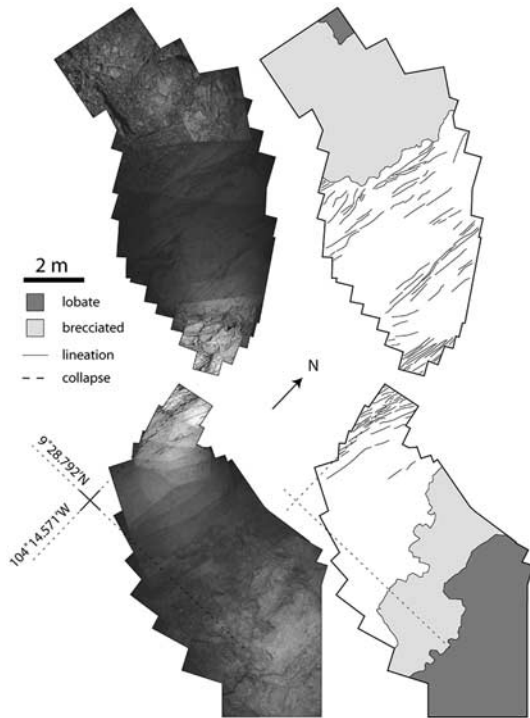
**Figure 10.** (left) Mosaic of digital still images from a downlooking camera mounted on *Alvin* and (right) interpretation of the mosaic. This transect, D, is from the southern channel system at 9°28′N and shows wide brecciated margins and a heavily lineated central sheet.

in the emplacement of each channel influenced by differing eruption properties or pre-eruption terrain. We conducted first-order modeling of flow through the channels to investigate differences in the eruption parameters that could lead to surface morphology variations.

## 5. Modeling

[21] With estimates of channel depth and width from high-resolution bathymetry and well-constrained assumptions regarding lava rheology [e.g., *Spera*, 2000] we are able to determine the velocity field for gravity driven flow of the lava within each channel using a 3D solution to the Navier-Stokes equation [*Tallarico and Dragoni*, 1999]. As lava samples from within the channel are glassy and nearly aphyric, we assume that the lava behaves as a Newtonian fluid for most of its flow history. We use microprobe analyses and the thermodynamic modeling program MELTS [*Ghiorso and Sack*, 1995; *Asimow and Ghiorso*, 1998] to determine lava density ($\rho = 2680$ kg/m$^3$) and viscosity ($\eta = 400$ Pa s), and assume that the flow is isothermal and thus of uniform $\eta$ and $\rho$. In addition, we assume that the lava is incompressible,

flow is laminar, that the channel has a rectangular cross section, and we impose no-slip (i.e., lava velocity goes to zero) boundaries at the sidewalls and base. This allows us to simplify the Navier-Stokes equation to

$$\eta\left(\frac{\partial^2 v_x}{\partial y^2} + \frac{\partial^2 v_x}{\partial z^2}\right) = \rho g \sin\alpha, \qquad (1)$$

where $v_x$ is the velocity in the down flow direction, $g$ is the acceleration due to gravity, and $\alpha$ is the slope [*Landau and Lifchitz*, 1971]. A general series solution to equation (1) developed to solve analogous equations for torsion in a rectangular beam [*Timoshenko and Goodier*, 1951; *Knudsen and Katz*, 1958; *Batchelor*, 1967] is

$$v_x(y,z) = \frac{16d^2}{\pi^3}\frac{\rho g' \sin\alpha}{\eta}\sum_{n=1,3,5}^{\infty}\frac{1}{n^3}(-1)^{(n-1)/2}$$
$$\cdot\left[1 - \frac{\cosh(n\pi y/2d)}{\cosh(n\pi a/4d)}\right]\cos\frac{n\pi z}{2d}, \qquad (2)$$

where $a$ is channel width, $d$ is channel depth, and $g'$ is the reduced gravitational acceleration due to eruption in water rather than air ($g' = g\Delta\rho/\rho$; $\Delta\rho = \rho_{lava} - \rho_{water}$).
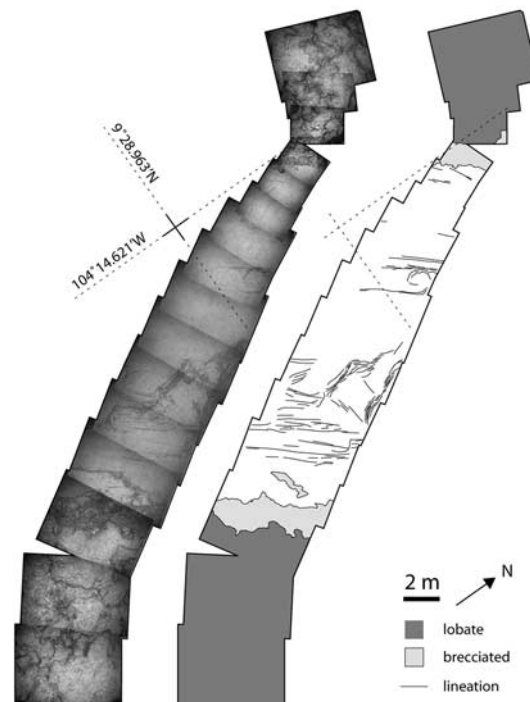


**Figure 11.** (left) Mosaic of digital still images from a downlooking camera mounted on *Alvin* and (right) interpretation of the mosaic. This transect, K, is from the northern channel system at 9°28′N and shows narrow brecciated margins and a moderately lineated central sheet.
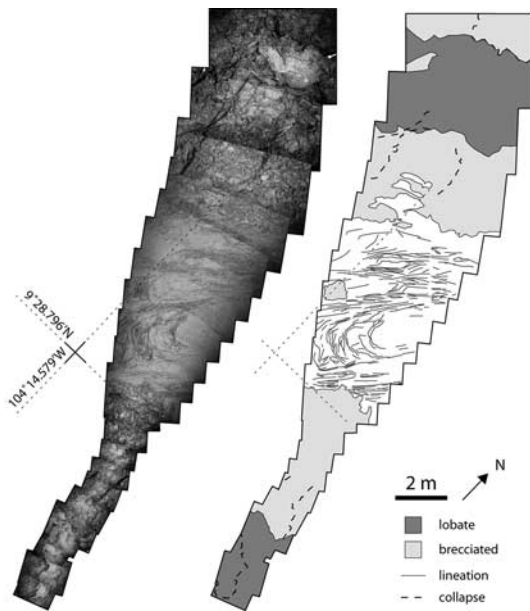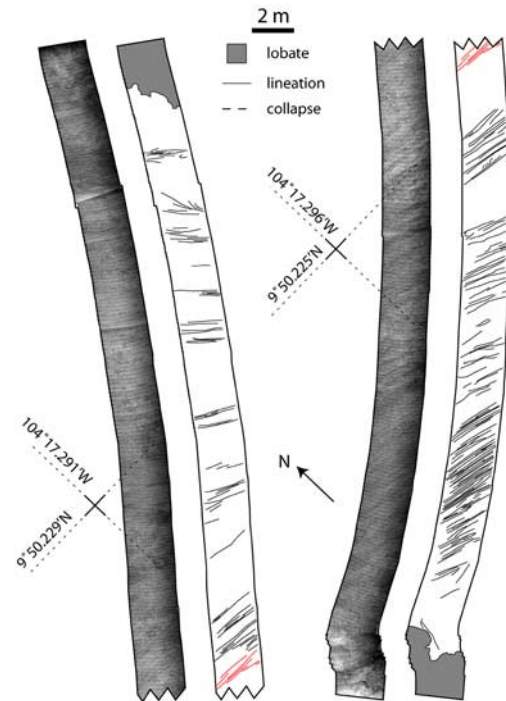
**Figure 12.** (left) Mosaic of digital still images from a downlooking camera mounted on *Alvin* and (right) interpretation of the mosaic. This transect, L, is from the northern channel system at 9°28′N and shows narrow brecciated margins and a sparsely lineated central sheet.
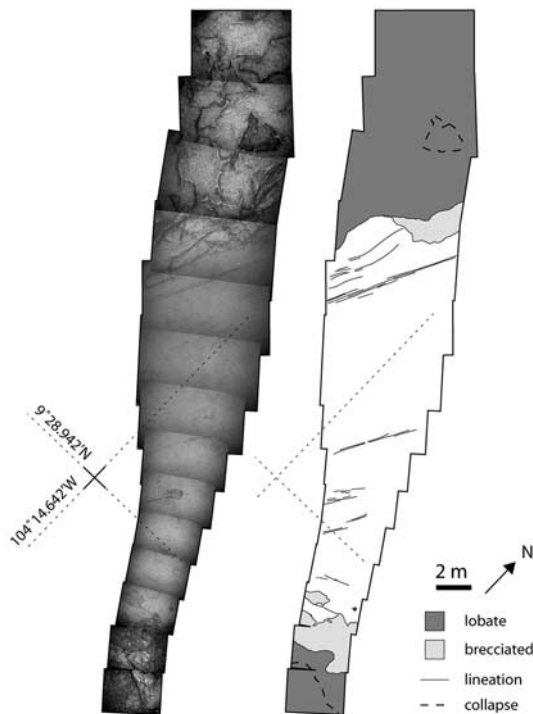


**Figure 13.** (left) Mosaic of digital still images from a downlooking camera mounted on *Alvin* and (right) interpretation of the mosaic. This transect, M, is from the northern channel system at 9°28′N and shows narrow brecciated margins and a sparsely lineated central sheet.



**Figure 14.** (left) Mosaic of digital video stills from a camera mounted on *Alvin* and (right) interpretation of the mosaic. This transect, P, is from the channel system at 9°50′N and shows no brecciated margins and a moderately lineated central sheet. The mosaic is broken into two parts. The red lineations indicate the same location on each section of the mosaic.

[22] Results of the modeling are shown in Table 4. The parabolic form of the resulting velocity field (Figure 15) is controlled by no-slip boundaries at the channel walls. The maximum velocity is sensitive to the channel dimensions, particularly depth. Using seafloor slopes common to the EPR crest (1–3°) results in a range of maximum velocities from 2.6–8.6 m/s for the shallowest (P) and deepest (C) channels respectively. Shear rates determined from the slope of the velocity profile are greatest at the channel margins and smallest at the channel center (Figure 15). Flux through the channel is determined by integrating the velocity distribution over the height and width of the channel with the following equation derived by *Tallarico and Dragoni* [1999]:

$$Q = \frac{\rho^2 g' \sin\alpha}{3\eta} ad^3 \left(1 - \frac{384}{\pi^5} \frac{d}{a} \sum_{n=1,3,5\ldots}^{\infty} \frac{1}{n^5} \tanh\frac{n\pi a}{4d}\right). \quad (3)$$

[23] Our maximum model velocity of 8.55 m/s and flux of $4.83 \times 10^3$ m³/s are considerably less than those predicted by *Sakimoto and Gregg* [2001] for submarine lava channels (v = 151 m/s; Q = $8.9 \times 10^3$ m³/s). Small differences in estimates of lava viscosity and density make a modest contribution

**Table 3.** Mosaic Descriptions

| Mosaic[a] | Channel Width, m | Morphologies Present (N-S)[b] | Brecciated Zone (N)[c] | Brecciated Zone (S) | Brecciated Zone (Ave.) | Description |
|---|---|---|---|---|---|---|
| B | 16 | L-B-S-B-L | 5.64 (0.35) | 3.37 (0.21) | 0.28 | Central flat sheet is densely lineated and contains are region of cuspate folds reminiscent of Hawaiian pahoehoe lava flows. |
| D | 17 | L-B-S-B-L | 4.52 (0.27) | 2.28 (0.13) | 0.20 | Small gap in center of mosaic due to low altitude of *Alvin*. Central flat sheet is moderately lineated with dense concentrations at the center and southern margin of the sheet. |
| K | 35 | L-B-S-B-L | 3.06 (0.09) | 2.52 (0.07) | 0.08 | Central flat sheet is moderately lineated with concentrations at the northern margin, but a wide featureless central portion. Lineations become more convoluted approaching the channel center. |
| L | 34 | L-B-S-B-L | 2.93 (0.09) | 1.44 (0.04) | 0.06 | Central flat sheet is sparsely lineated by narrow (20 cm) bands of dense lineations separating wide (∼1 m) featureless regions. |
| M | 24 | L-B-S-B-L | 0.85 (0.04) | 1.63 (0.07) | 0.05 | Central flat sheet is sparsely lineated and free of lineations in the central region. |
| P | 36 | L-S-L | 0 | 0 | N/A | Central sheet is moderately lineated. Lack of brecciated zones may result from being covered by later lava flows. |

[a] Mosaic indicators correspond to transects shown in Figure 8.
[b] Morphology indicators are as follows: L, lobate; B, brecciated; S, sheet.
[c] Widths of brecciated zones are in meters. Widths normalized to total channel width are shown parenthetically.

to this difference. More important are differences in channel dimensions. *Sakimoto and Gregg* [2001] report channel depths from 2–8 m that were obtained with altimetry and depth sensor data from *Alvin* dives (T. K. Gregg, personal communication, 2004). *Cormier et al.* [2003] report depths of <2 m and we find depths <3 m determined by high-resolution bathymetry or in situ observations. An additional difference is in the reported slopes. Again, the range of slopes used by *Sakimoto and Gregg* [2001] of 1 to 8° are significantly greater than those reported by *Cormier et al.* [2003] of 1.8° and those we have determined (1 to 3°) on the basis of near-bottom sonar data. The modeling reported

here, using refined estimates of channel dimensions and local slope provide better constraints on channel flow velocities and flux.

## 6. Discussion

### 6.1. Relationship Between Surface Morphology and Modeled Flow

[24] The observed surface morphology pattern on submarine channels is similar to that which is observed in subaerial lava channels where the morphology of the central portion of the channel is pahoehoe and the margins are ′a′a [e.g.,

**Table 4.** Results of Numerical Modeling of Flow Through a Rectangular Channel

| Channel Transect | Depth, m | Width, m | Viscosity, Pa s | Density, kg/m$^3$ | Velocity Max, m/s | Shear Rate Max, s$^{-1}$ | Flux, m$^3$/s |
|---|---|---|---|---|---|---|---|
| B | 2.9 | 23 | 400 | 2680 | 8.55 | 4.37 | $4.83 \times 10^3$ |
| D | 1.9 | 18 | 400 | 2680 | 3.68 | 2.86 | $1.10 \times 10^3$ |
| K | 2.18 | 42 | 400 | 2680 | 4.85 | 3.26 | $1.50 \times 10^3$ |
| L | 2.05 | 40 | 400 | 2680 | 4.29 | 3.07 | $4.17 \times 10^3$ |
| M | 2.08 | 40 | 400 | 2680 | 4.42 | 3.12 | $3.44 \times 10^3$ |
| P | 1.6 | 36 | 400 | 2680 | 2.61 | 2.39 | $0.39 \times 10^3$ |
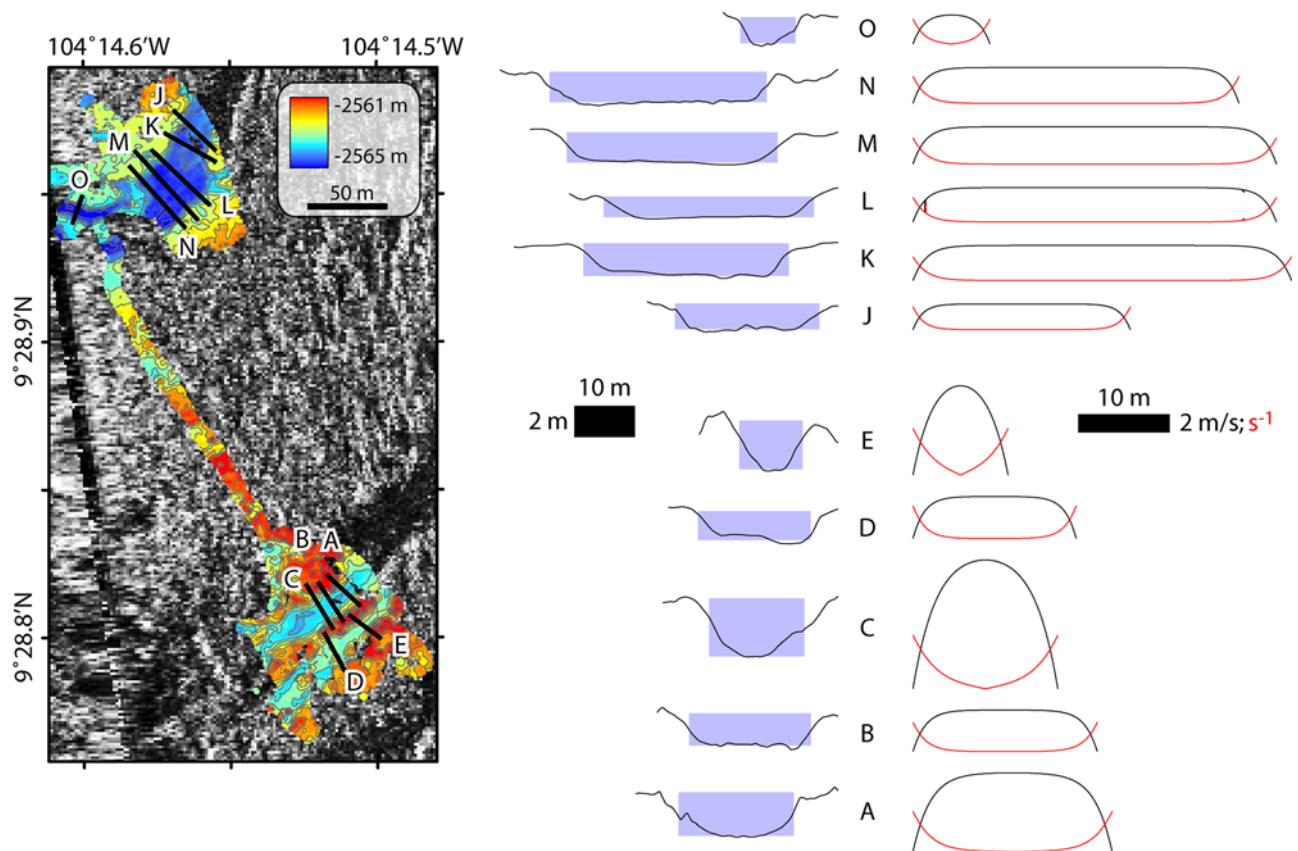
**Figure 15.** (left) Very high-resolution (50 cm horizontal and 10 cm vertical) microbathymetry, compiled from 675 kHz scanning altimetry collected from *Alvin*, covering the northern and southern channel systems at 9°28′N and 0.5 m contours plotted on sonar backscatter imagery. (middle) Bathymetric profiles over channels are shown with shaded boxes indicating the dimensions of channels used in modeling. Modeled velocity (black) and shear rate profiles (red) across the channels are shown at right. Scales for channel dimensions velocity and shear rate profiles are shown by black boxes. Values for channel dimensions with accompanying mosaics, maximum velocity, and shear rate are shown in Table 4.

*Kilburn*, 1990; *Soule et al.*, 2004]. In the subaerial environment, this surface morphology distribution is controlled by variations in shear rate across the channel, which are greatest at the channel margin and smallest at the channel center [e.g., *Kilburn*, 1990]. A distinct difference between the two environments, however, is that in the submarine environment the marginal brecciated zone is formed by deformation of solidified crust, whereas in the subaerial environment, it is deformation of subsolidus lava that produces ′a′a [e.g., *Soule and Cashman*, 2005]. The similarity in distribution of analogous surface morphologies suggests that a correlation between shear rate and width of the brecciated zone may be present for submarine lava channels [*Griffiths et al.*, 2003]. Another possibility is that the brecciated zones form post-emplacement due to bending of the surface crust as the lava drains and the crust sags.

[25] If the former is true, then there should be a threshold shear rate, above which the crust brecciates and below which it remains intact. Assuming that the material properties of solidified crusts (including crust thickness) are not dramatically different in each of the submarine environments where we have measured the width of the brecciated zone (BZ), we can then determine the threshold shear rate from our model of velocity across the channel. Figure 16 shows BZ widths measured from mosaics versus BZ widths predicted for a variety of threshold shear rates from our flow model results. We find that a range of shear rates ($\dot{\gamma} = 0.28 - 0.75$ s$^{-1}$) are needed to describe BZ width on the northern channels at 9°28′N, whereas a single shear rate of $\dot{\gamma} = 0.15$ s$^{-1}$ can predict the BZ widths on the channels of the southern system at 9°28′N. Thus we propose that wide BZ relative to total channel width, such as on the southern channels at 9°28′N form during emplacement due
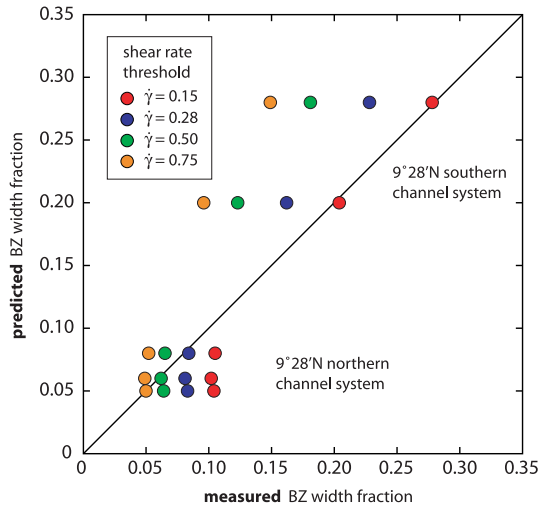
**Figure 16.** Measured width of the marginal brecciated zone (BZ) versus width predicted from modeled shear rate within the channel given a threshold shear rate. Large symbols indicate agreement between measured and predicted widths. A single threshold shear rate $(0.15\ \text{s}^{-1})$ can explain BZ widths for the southern channel system at 9°28′N, whereas a large range of threshold shear rates $(0.28–0.75\ \text{s}^{-1})$ is needed to explain BZ widths in the northern channel system at 9°28′N.

to high shear rates at the channel margins. We suggest that narrow BZ, such as on the northern channels at 9°28′N, formed after emplacement due to bending of the surface crust as the channel was drained of lava.

[26] During emplacement these two styles of channelized flow emplacement would differ in the degree of crust coverage, with open, uncrusted margins on wide BZ channels and complete crust coverage on narrow BZ channels. Similar morphologies are evident in physical models using an analog fluid (PEG 600) to represent lava with a solidifying crust and are termed "tubes" and "mobile crust" [*Griffiths et al.*, 2003]. In these experiments PEG 600, above its liquidus, was extruded into a cold sucrose solution and allowed to flow down a rectangular channel over a 3.5° slope. In some experiments, shear zones at the margins of the channel were open (i.e., crust-free) allowing a smooth, "mobile crust" to travel down the center of the channel. In other experiments, the solidifying crust at the margins was not broken and the surface crust extended across the channel, from margin to margin, creating a "tube." As with our results, *Griffiths et al.* [2003] did not find a single threshold shear rate where the transition from a crusted to open margin occurred. However, they

did find that convection within the channel that delivered hot material from the channel center to the channel margins played an important role. They were able to develop a relationship between the Rayleigh (*Ra*) number of the flow and the dimensionless parameter Ψ, a ratio of the timescale of solidification to the timescale of advection. Using direct observations of channel dimensions from high-resolution bathymetry, we calculated *Ra* number as

$$Ra = g\varepsilon(\Delta T)d^3/\kappa\nu, \qquad (4)$$

where $\varepsilon$ is thermal expansion coefficient of basalt $(6 \times 10^{-5}\ \text{K}^{-1}$ [*Phillpotts*, 1990]), $\Delta T$ is the difference between the lava temperature and solidification temperature, $d$ is channel depth, $\kappa$ is thermal diffusivity $(5 \times 10^{-7}\ \text{m}^2/\text{s}$ [*Williams and McBirney*, 1979]), and $\nu$ is kinematic viscosity $(\nu \equiv \eta/\rho$, where $\rho$ is 2680 kg m$^{-3}$). We calculated Ψ,

$$\Psi = \tau_\sigma/\tau_\alpha, \qquad (5)$$

using estimates of the solidification timescale $(t_s = 0.07\ \text{s}$ [*Fink and Griffiths*, 1992]) and the advection timescale $(t_a = v_x/d$, where $v_x$ is the mean velocity determined by equation (2)).

[27] Our model of flow through the channel assumed that the lava was isothermal, a necessary constraint to analytically solve for the flow field. However, we recognize that the flow will be thermally stratified, with the upper surface having a temperature somewhere between that of the liquid lava and the ambient seawater. This vertical temperature gradient, if large enough, will give rise to thermal convection within the flow. Thermal gradients, although expected, have not been measured in subaerial or submarine lava channels. Although utilizing *Ra* violates our assumption of isothermal flow from our velocity model, it is a necessary first step in investigating the relationship between empirical models and field observations of submarine lava flows.

[28] We have determined Ψ and *Ra* for the channelized flows in our study area using our derived velocity estimates. We find that our results recreate the form of the relationship observed in analog experiments of *Griffiths et al.* [2003], and that channels that show characteristics of the "mobile crust" (wide BZ) or "tube" (narrow BZ) regime plot within their empirically defined fields (Figure 17). Scaling between the two materials, especially the solidified PEG and lava, remains unresolved [*Soule and Cashman*,
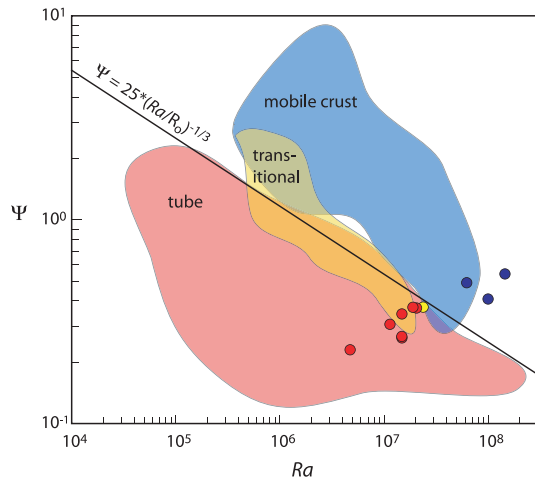
**Figure 17.** Relationship between channels that form "mobile crust" and "tube" morphologies derived from analog experiments by *Griffiths et al.* [2003]. Circles show modeled *Ra* and Ψ for channels from the 9°28′N region of the EPR, and their color indicates observed or inferred crust regime.

2004], however, the agreement between the analog and natural flows gives us confidence that our inference of volume flux derived from modeling gravity driven flow through channels is reasonable. The volume flux we determined, $0.4 – 4.8 \times 10^3$ m³/s, falls within the bounds for effusion rates of channelized flows at the SEPR ($10^2$ to $10^4$ m³/s) suggested by *Sakimoto and Gregg* [2001].

## 6.2. Origin of Channelized Flows

[29] From side-scan sonar maps, it is clear that many channelized flows in the EPR study area originate at the AST, presumably as lava filled and overflowed the AST (Figure 3) [*Fornari et al.*, 1998, 2004]. However, some channels, including those that we have sampled for this study, initiate 50–300 m from the AST. This latter group of channels was either erupted off-axis, where we observe the first expression of the channel, or erupted at the AST and did not form a channel at the eruption site, or their proximal (near-AST) channels have not been preserved (i.e., were covered by later flows). We utilize the geochemistry of samples from channels that first appear some distance from the AST to constrain the location of their eruption. In addition, their geochemistry aids the interpretation of lava contacts that are unclear in side-scan imagery and our resulting interpretation of the style of eruptions that lead to channelized flows at 9°50′N and 9°28′N.

[30] The fast spreading EPR is characterized geochemically by more primitive melts erupting from the AST relative to off-axis eruptions at the same latitude [e.g., *Langmuir et al.*, 1986, 1992; *Reynolds et al.*, 1992; *Perfit et al.*, 1994; *Reynolds and Langmuir*, 2000; *Smith et al.*, 2001]. On the EPR from 9°–10°N, lava geochemistry varies latitudinally with more evolved lava (Mg# ∼ 0.55– 0.60) south of the 9°37′N overlapping spreading center (OSC), and more primitive lava (Mg# ∼0.60–0.68) north of the OSC (Figure 18) [*Langmuir et al.*, 1986; *Smith et al.*, 2001]. In general, eruptions that occur 1–∼3 km from the AST have lower Mg#, which is believed to result from tapping the cooler, more evolved wings of the magma chamber and smaller lenses within the mush zone [*Perfit et al.*, 1994; *Perfit and Chadwick*, 1998]. Mg# from the channel samples we analyzed are plotted in Figure 18 and their chemistry is typical of eruptions within the AST at each location (Mg# = 0.588 ± 0.004 at 9°28′N; Mg# = 0.654 ± 0.007 at 9°50′N). In addition K/Ti ($K_2O/TiO_2*100$), which serves as a petrogenetic discriminant of magma enrichment [e.g., *Langmuir et al.*, 1986; *Rubin et al.*, 2001; *Perfit et al.*, 1994; *Reynolds and Langmuir*, 2000] is 7.6 ± 0.7, within the field defined for axially erupted EPR lavas [*Smith et al.*, 2001]. Thus it appears that channelized flows, even those that appear to initiate 50–300 m from the AST, were erupted from the AST.

[31] Despite the AST-like geochemical signature of lava within the channel, lava channels at 9°50′N first appear ∼150 m from the AST. This inconsistency is explained by the proximal channel being covered by a later flow. Photographic and observational evidence shows lobate lava overriding the flat sheets of the channel. Covariation of major oxide species (CaO, $Na_2O$, and FeO) relative to MgO of samples from within and adjacent the channel and samples of the lobate lava at the head of the channel are distinct and support this observation. The proximal, channel covering lava overlaps compositionally with the 1991 Barbeque flow [*Gregg et al.*, 1996] that locally overflowed the AST in approximately the same location (Figure 19). Whereas photographic and visual observations are unequivocal as to the timing of emplacement (http://4dgeo.whoi.edu/DAQ/AT11-07/dive_list.html) the geochemical evidence can only suggest that the channel lava and proximal, channel-covering lava represent different eruptions.

[32] At 9°28′N, channels initiate 50–150 m from the AST and are bound by lobate lava that is
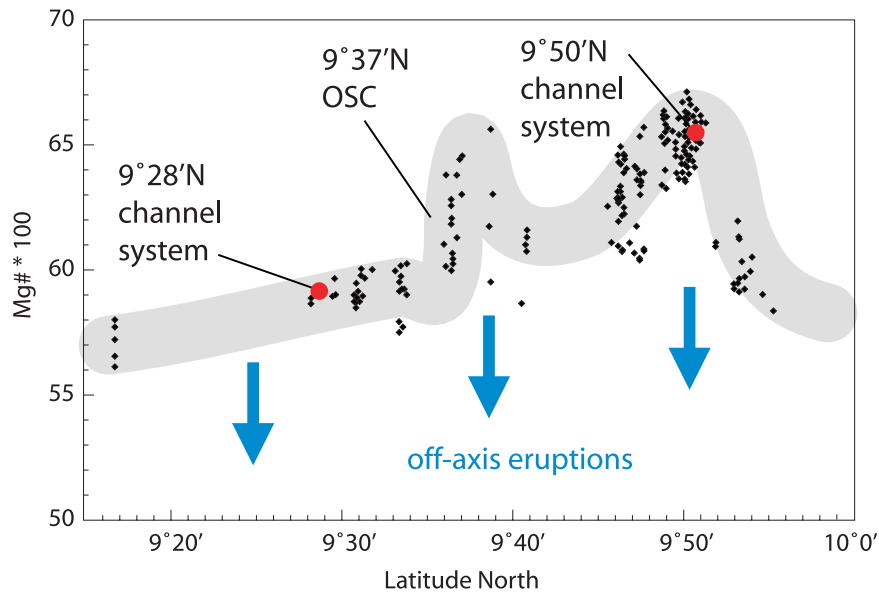
**Figure 18.** Mg# of axial lava samples (black diamonds) from 9°15′N to 10°N on the EPR compiled by *Smith et al.* [2001]. Average Mg# for channel samples are shown in red and plot on the axial Mg# curve. Off-axis eruptions tend to have lower Mg# as indicated by blue arrows [*Perfit and Chadwick*, 1998; Perfit et al., manuscript in preparation, 2005].

chemically indistinguishable from channel material. The same is true of samples collected in this area along a complex channel system, where multiple channels are present and segments of channels are not visibly connected (Figure 20). At this location, there is no evidence for later flows covering the proximal portions of the channels. Instead, it appears from acoustic texture, micro-bathymetry, and visual observations that the near-axis region at 9°28′N is heavily collapsed. It is possible that evidence of the channels near the vent was obscured by collapse, or that the initial axis overflow produced lobate flows that eventually coalesced into channels and the subsequent down-flow draining of lava through the channels led to the collapse.

[33] We conclude that channelized flows at both 9°50′N and 9°28′N were erupted at the AST; however, the style of those eruptions may have differed. At 9°50′N the primary channels are distinct from one another and adjacent lava flows have slightly different compositions. At 9°28′N, many channels are present on the west side of the AST along a ∼5 km section of the ridge and many of those channels merge with one another down-slope suggesting a large, coeval eruptive event. In addition, despite apparent contacts between adjacent flows at 9°28′N in side-scan imagery, inter-flow chemical compositions do not vary. Thus we suggest that lava channels at 9°28′N resulted from a longer active fissure, greater volume flux, and

longer eruption duration than the eruption(s) that produced the 9°50′N lava channels. This is supported by the estimated flux determined for individual channels from modeling (see Table 4). Eruption rates for this event will depend on the number of channels and length of fissure that was active at any one time during the eruption. The eruption may have initially advanced as a sheet within which channels subsequently developed as suggested by *Ryan et al.* [1999] for channels at 17°28′S on the EPR. The character of the 9°28′N eruption agrees with the interpretation of *Sinton et al.* [2002] of large lava flows on the southern EPR that were emplaced episodically over periods of years to decades in a fashion analogous to the current Pu'u 'O'o-Kupaianaha eruption of Kilauea Volcano that has been emplaced in >50 discrete episodes over a period of 20 years [*Heliker and Mattox*, 2003].

### 6.3. Regional Channel Distribution

[34] Except for small portions of the S. EPR [*Sinton et al.*, 2002], JdFR [*Chadwick et al.*, 2001], and Mid-Atlantic Ridge MAR [*Scheirer et al.*, 2000; *Bohnenstiehl and Kleinrock*, 2000], no other ridge crest has the comprehensive along- and off-axis, high-resolution (2 m) side-scan and complementary microbathymetry coverage necessary to accurately map channelized lava flows, and none do so over ridge lengths spanning multiple segment
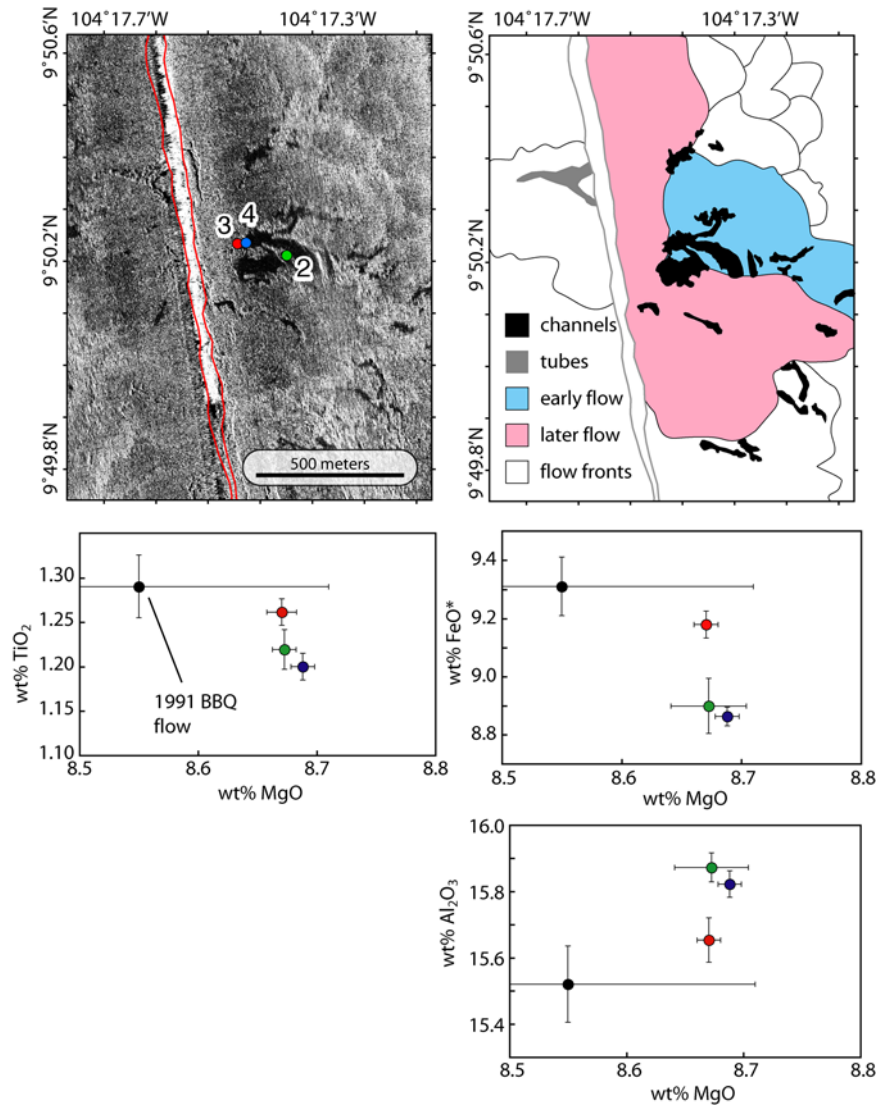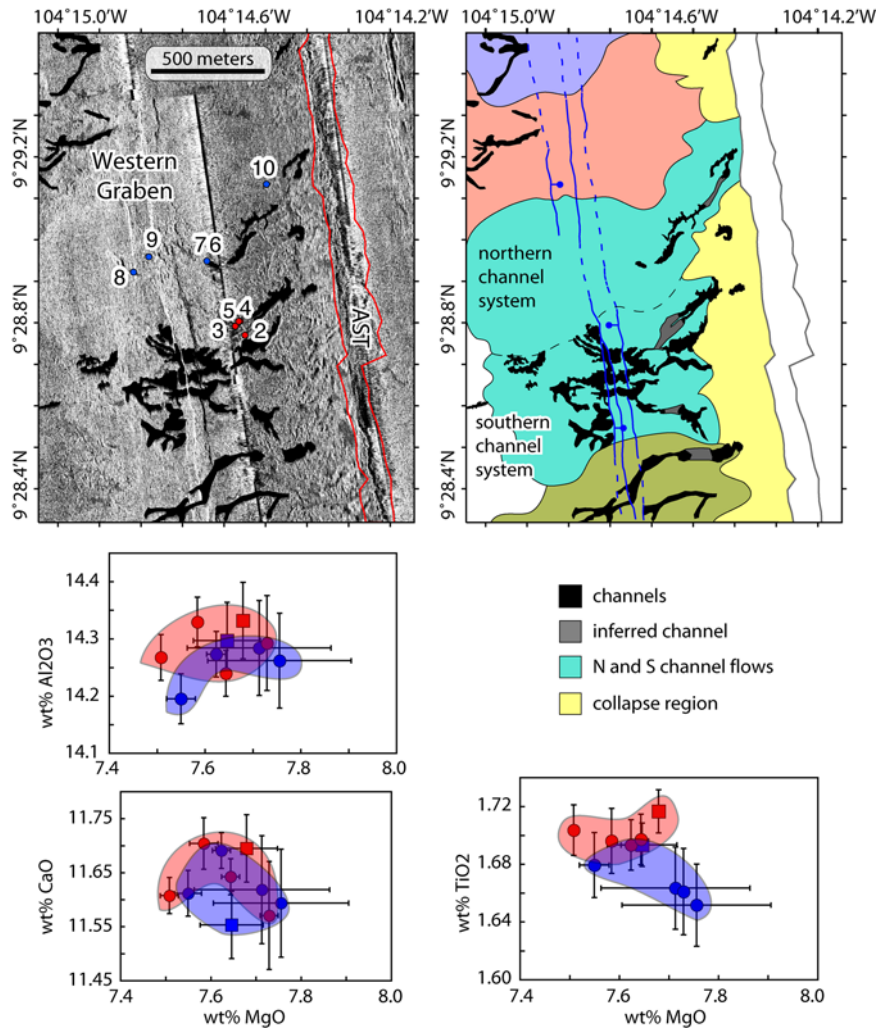
**Figure 19.** (top left) Side-scan sonar map of channels at 9°50′N and (top right) geological interpretation show that the proximal portion of channels that originate 100–200 m from the axis were covered by later lavas of slightly different composition. Compositions are shown in Harker diagrams where symbol colors correspond to symbols in side-scan map relative to the composition of the 1991 BBQ flow [*Gregg et al.*, 1996]. Outline of AST shown in red on sonar map and as gray line on interpreted geology.

boundaries. This provides us a unique opportunity to investigate how variations in the volcanic character of the ridge, in this case, the presence of channelized flows, impacts crustal accretion processes as determined by independent geophysical and observation methods. Along the ∼60 km of EPR ridge axis from 9°25′N–10°N, channelized lava flows are common, numbering ∼300. The distribution of channels along and across the ridge, however, is variable (Figure 21). As we have shown, channelized lava flows reflect high-effusion-rate ($10^3$ m$^3$/s), high-velocity eruptions that originate at the AST and are capable of transporting and depositing lava 1–3 km from the trough. Thus,

as a first-order hypothesis, we expect greater lava accumulation in the off-axis region and consequently greater thickening in layer 2A in areas having a high concentration of channelized lava flows.

[35] Figure 21 shows the across- and along-axis distribution of channelized flows determined from the surface area fraction of channels relative to other flow types (i.e., lobate and pillow flows). Surface area fraction is determined from slices of a binary map of channelized flows (black) and all other surfaces (gray) in equidistant segments. The shape of the AST (across-axis) or latitudinal lines

**Figure 20.** (top left) Side-scan sonar map and (top right) geologic interpretation of channels at 9°28′N. Samples along the northern channel system (blue dots) do not vary in composition, nor do samples from the two distinct channel systems (north and south). These two systems do represent eruptions separated by some time as the latter (northern) covers channels in the former (southern). Proximal expressions of the channels were destroyed by wholesale collapse of an inflated AST overflow. Additional flows are shown in other colors. (bottom) Harker diagrams show that the major element variability between samples collected from the northern (blue) and southern (red) channel systems are negligible. Outline of AST shown in red on sonar map and as gray line on interpreted geology.

(along-axis) define the slice boundaries. The cross-axis distribution of channels shows a Gaussian distribution with a peak near the AST that decays rapidly within 2–2.5 km of the axis. Across-axis channel distributions are slightly asymmetric, with the greatest channel abundance east of the AST in the 9°50′N area and west of the AST south of the 9°37′N OSC. Channels are variably distributed along the ridge axis with several peaks in channel density (Figure 21). The peak at 9°25′–30′N is the most striking, with a four-fold increase in average channel density relative to the rest of the ridge. Those at 9°50′N and 9°43′N are less dramatic

displaying 1.5–2 times the background channel density.

### 6.3.1. Ridge Crest Geometry

[36] The cross-axis shape of the EPR ridge crest (triangular, domed, or rectangular) can be influenced by a number of different volcanic and tectonic processes including accretion of extruded lava, magma chamber inflation/deflation, faulting, thermal budget, [e.g., *Macdonald and Fox*, 1988; *Scheirer and Macdonald*, 1993] or geometry of the Layer 2A–2B boundary [*Carbotte et al.*, 1997].
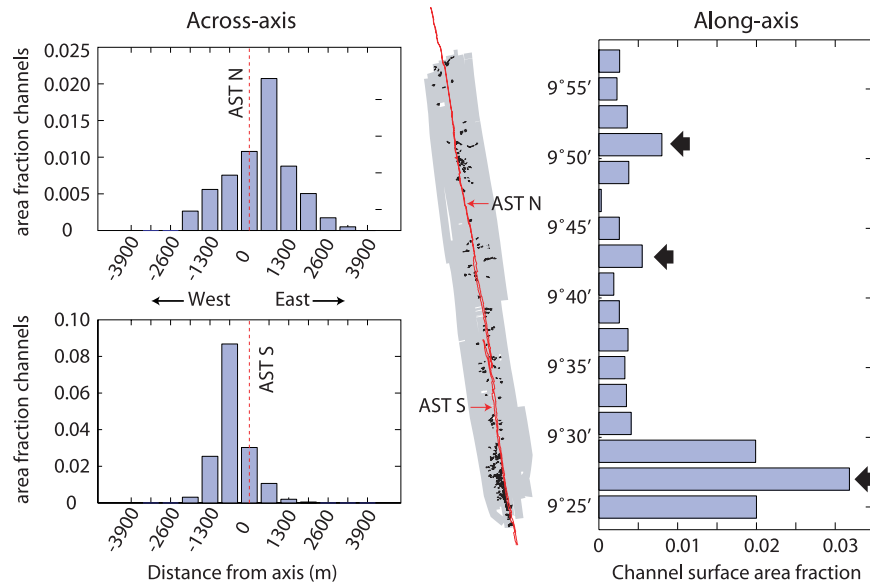
**Figure 21.** (left) Cross-axis and (right) along-axis channel distribution is determined by measuring the surface area comprised by channels in slices of the ridge axis defined by either the boundary of the AST or latitudinal lines. Cross-axis distribution of channels is Gaussian with peaks in channel density just east and west of the AST to the north and south of the 9°37′N overlapping spreading center. Along axis channel density is greatest at 9°28′N by at least a factor of four over the rest of the ridge in the study area. Smaller peaks in channel density are apparent at 9°50′N and 9°43′N (arrows).

Although classifying the ridge crest shape is somewhat subjective, clear distinctions in shape and cross-sectional area have been reasonably correlated with magma budget inferred from high-temperature venting, recent eruption, and seismic evidence of a shallow magma chamber. Rectangular ridges indicate greater magma budget, domed ridges indicate intermediate magma budget, and triangular ridges indicate decreased magma budget [*Macdonald and Fox*, 1988; *Scheirer and Macdonald*, 1992; *Carbotte et al.*, 1997].

[37] We use multibeam bathymetry data collected by *Cochran et al.* [1999] to determine the shape of the upper 350 m of the ridge crest. At this section of the EPR, the ridge crest is domed-shaped over most of its length, indicating a robust magma budget [e.g., *Macdonald and Fox*, 1988]. However, a portion of the ridge from 9°17′N–9°33′N is rectangular-shaped, indicating an elevated magma budget. *Fornari et al.* [1998] also found that the area between ∼9°14′–21′N had been recently paved over by an eruption that filled the AST. They speculated, on the basis of observational data related to hydrothermal vent fluid chemistry [*Von Damm et al.*, 1997] and animal communities near 9°17′N [*Shank et al.*, 1998], that the eruption may have occurred between 1987–1989. This portion of the ridge also has the greatest channel density,

which raises the question of whether or not the anomalous volcanic accretion reflected by the channels has influenced the cross-axis shape.

[38] We gain some insight into this question by examining ridge-crest asymmetry. We divide the cross-sectional area of the ridge crest in our study area, not influenced by faulting, in two parts at the AST and examine those areas relative to each other. Figure 22 shows the results of that analysis for twelve cross-ridge transects. We find that peaks in ridge asymmetry correlate with both the position and magnitude of peaks in along-axis channel density. The greatest asymmetry is at 9°28′N, where the cross-sectional area of the ridge crest is more than two times greater to the west of the AST than to the east. In this area, nearly all the channels transport lava to the west of the axis suggesting that this type of flow can have a dramatic impact on where lava is distributed across the ridge crest. However, it should be noted that compliance measurements at this location indicate the shallow melt lens is centered just west of the AST [*Crawford and Webb*, 2002]. Although the volcanic evidence suggests that most volcanic eruptions at 9°28′N occur at the AST, the thermal structure resulting from an offset melt lens may also impact the gross features of the ridge crest [e.g., *Carbotte et al.*, 1997]. From this data, we conclude that volcanic
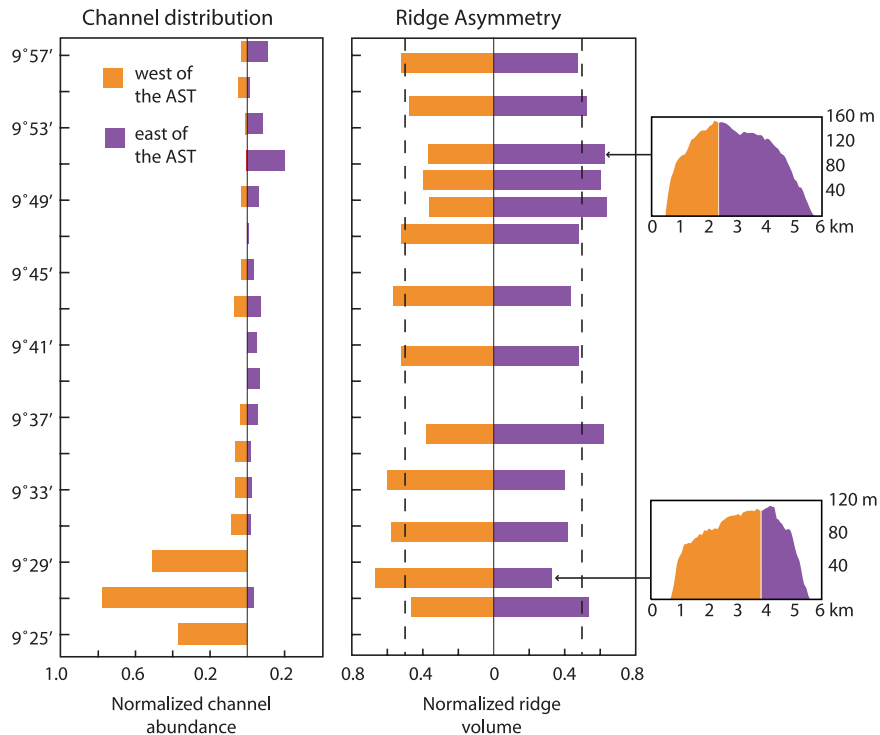
**Figure 22.** (left) Along-axis channel abundance is normalized to the maximum channel abundance and is shown as a combination of orange (west of the AST) and purple (east of the AST) bars. (right) Channel abundance correlates with ridge-crest asymmetry. Ridge volume on either side of the AST is normalized to one. A bar that falls between the dashed lines is perfectly symmetrical. Examples of ridge-crest profiles are shown at the far right. The greatest asymmetry is at $9°28'$N. Smaller, but significant, asymmetry is found at $9°43'$N and $9°50'$N.

accretion, especially through channelized flows cannot be ruled out as a means of altering the ridge crest morphology, and that the surface expression of volcanism described in this study may reflect longer timescale accretion processes.

[39] We do not have direct measurements of the volume of material erupted or duration of submarine channelized lava flows. However, with some assumptions we are able to infer maximum volumes and durations for comparison to other submarine and analogous subaerial eruptions. We assume that all the excess material on one side of the ridge crest (Figure 22) is delivered through the channel systems visible at the surface, and that ridge crest asymmetry is similar 500 m to either side of measured ridge crest profiles. At $9°28'$N an additional $1.26-1.34 \times 10^8$ m$^3$ of lava was deposited west of the AST. At $9°50'$N, an additional $1.42-1.57 \times 10^8$ m$^3$ of lava was deposited to the east of the AST. The four distinct channel systems present at each location would have had to erupt $\sim3-4 \times 10^7$ m$^3$ of lava to account for the excess volume. We recognize that these volumes are almost certainly overestimates of actual flow volumes as it is unlikely that all the excess

material has been delivered by the relatively few channels we can see at the seafloor surface. Indeed, the resulting volume estimates are an order of magnitude greater than those inferred by *Sinton et al.* [2002] for large eruptions on the southern EPR, the 1998 Axial Volcano eruption [*Fox et al.*, 2001], as well as the 1991–92 BBQ flow at $9°50'$N [*Gregg et al.*, 1996; *Perfit and Chadwick*, 1998]. However, these volumes are similar to estimates from individual flows at intermediate spreading rate ridges ($1-9 \times 10^7$ m$^3$) [*Embley and Chadwick*, 1994; *Chadwick et al.*, 2001] and slow spreading ridges ($4-80 \times 10^7$ m$^3$) [*Crane and Ballard*, 1981; *Smith and Cann*, 1990; *Bryan et al.*, 1994], although the form of erupted lava, constructional pillow mounds, is dissimilar.

[40] The inferred volumes for these channelized flows can be used to infer eruption durations of 9–10 hours using our modeled volume fluxes. This duration is similar to that of comparably sized eruptions from Kilauea Volcano, Mauna Loa Volcano, and in Iceland which generally last 2–>24 hours [e.g., *Wolfe et al.*, 1988; *Lockwood et al.*, 1987; *Thordarsson and Self*, 1993]. This duration estimate, however, is 3–5 times greater

**Table 5.** Layer 2A Properties as Determined From *Harding et al.* [1993]

| Latitude | Channel Density | Ridge Asymmetry | 2A thickness (distance) | | |
| | | | Axis | West | East |
|---|---|---|---|---|---|
| 9°30′N | 0.03 | 200% (W) | 193 m | 418 m (2.65 km) | 345 m (1.45 km) |
| 9°40′N | 0.002 | 104% (W) | 230 m | 425 m (1.45 km) | 440 m (1.38 km) |
| 9°50′N | 0.01 | 150% (E) | 265 m | 533 m (2.05 km) | 467 m (1.57 km) |
| *High-Resolution Shallow Seismic Refraction [Sohn et al., 2004]* | | | | | |
| 9°50′N | 0.01 | 150% (E) | 20 m | 125 m (0.99 km) | 109 m (1.50 km) |

than the estimate for the AST filling 1991 eruption at 9°50′N on the EPR [*Gregg et al.*, 1996] and nearly an order of magnitude greater than the 1998 Axial Volcano eruption [*Fox et al.*, 2001], both of which were volumetrically smaller than our estimates for the channelized flows. Although speculative, these volume and duration estimates for northern EPR channelized lava flows are useful as constraints on maximum values and support the hypothesis that excess ridge crest volume can be achieved by extrusive lava accretion.

## 6.3.2. Layer 2A Thickening

[41] Seismic imaging of layer 2A [e.g., *Christeson et al.*, 1992; *Detrick et al.*, 1993; *Harding et al.*, 1993; *Vera and Diebold*, 1994; *Kent et al.*, 1994; *Carbotte et al.*, 1997] and near-bottom magnetic intensity measurements have been used to constrain stochastic models of volcanic construction at the EPR [e.g., *Hooft et al.*, 1996; *Schouten et al.*, 1999]. Those results indicate that lava deposition is bimodal; some lava flows are deposited within and up to 250 m from the AST, and some are deposited 1–3 km from the AST. Lava channels represent an efficient mechanism by which lava can be transported off-axis. We compare our observations of channel distribution (i.e., abundance) and ridge crest morphology to layer 2A structure as determined by seismic investigations within our study area. *Harding et al.* [1993] have imaged shallow crustal structure along cross-axis multichannel seismic lines at three locations that overlap our study area: 9°30′N, 9°40′N, and 9°50′N. *Sohn et al.* [2004] conducted on-bottom seismic refraction to produce layer 2A thickness maps at much finer resolution.

[42] Axial and off-axis thickness of layer 2A along with the width of the region of rapid 2A thickening are shown in Table 5. At 9°30′N, layer 2A achieves its maximum thickness, 2.2 times its axial thickness, at 2.7 km west of the AST. To the east of

the AST, layer 2A thickens 1.8 times at 1.5 km east of the AST. This asymmetric pattern of thickening correlates with the high abundance of lava channels west of the AST at 9°28′N (Figure 21) that results in part from the eastern rim of the AST being 1–3 m shallower than the western rim. At 9°40′N layer 2A thickens symmetrically to ∼2 times its axial thickness at 1.5 km both west and east of the AST. This symmetric thickening correlates with the lowest density of channels along this portion of the EPR and a symmetric cross-axis volume distribution on either side of the ridge crest (Figure 21). At 9°50′N, multichannel seismic [*Harding et al.*, 1993] and on-bottom seismic refraction [*Sohn et al.*, 2004] estimates of layer 2A thickness differ in the magnitude and direction (west or east of the AST) of layer 2A thickening. The length scale of channelized flow emplacement suggests that the higher-resolution refraction study is more relevant. In the *Sohn et al.* [2004] study layer 2A appears much thinner at the ridge crest and thickens >6 times (although only to a thickness of 125 m) within 1 km west of the AST, and >5 times within 1.5 km east of the AST, although the size of the seismic array may not resolve the final thickness of layer 2A. The greater width of the zone of layer 2A thickening east of the AST correlates with the greater abundance of channels east of the AST.

[43] Correlations between channel abundance and physical characteristics of the ridge crest suggest that crustal accretion by extrusive lava flows is important for creating the architecture of young oceanic crust. However, there is a discrepancy between the timescale of creating an asymmetric ridge crest and that of emplacing the channelized lava flows we observe at the seafloor surface. Surficial lava flows likely represent no more than 10 kyrs of volcanic activity based on the spreading age of the crust at the location of channel eruption sites and U-Th and Th-Ra disequilibria of lava samples collected in this region [*Goldstein et al.*,

1994; *Sims et al.*, 2003]. Ridge crest asymmetry, cross-axis shape, and layer 2A thickening likely represent on the order of 50–70 kyrs of activity on the basis of paleomagnetic spreading rates to the edge of the inflated ridge crest. Based on our findings that channelized flows erupt at the AST and are capable of transporting lava several kilometers off-axis, these correlations are not surprising if it is assumed that the surface expression of volcanism is maintained through the entire thickness of layer 2A. However, until we are able to investigate the detailed stratigraphy of the extrusive volcanic sequence, we will be unable to confirm the longer timescale (∼60 ka) volcanic evolution of this portion of the EPR that is implied by these apparent relationships.

## 7. Conclusions

[44] We have conducted a detailed investigation of a submarine lava flow type, channelized flows, which have only recently been identified through the collection of near-bottom, high-resolution sonar data sets. Channelized flows represent the high effusion rate and high flow advance rate member of the spectrum of submarine flow types as indicated by their unique surface morphology. As a result they provide a viable mechanism for transporting lava significant distances across the seafloor (observed to be at least 1–3 km) from the AST to the edges of the neovolcanic zone. An understanding of channelized lava flows provides valuable new insights into the process of crustal accretion at fast and superfast spreading ridges. From our observations, analyses, and interpretations we draw the following conclusions:

[45] 1. Over 300 lava channel segments can be distinguished within the neovolcanic zone of the EPR from 9°25′–10°N based on their low acoustic reflectivity in side-scan sonar maps and depressed topography in very high-resolution bathymetry. Observations of these channels during submersible dives confirm their presence and physical nature. Channels extend up to 3 km from the AST following paths dictated by the steepest slope and/or topographic obstructions.

[46] 2. Channels are hosted and created within lobate lava flows emplaced during the same eruption. A characteristic set of surface morphologies is present across all the channels we investigated. These include lobate lava up to the channel margins, a band of brecciated lava against the margins, and lineated or featureless sheets in the channel

center. The variable width of the brecciated zone between channels can be explained by formation due to flexure of the surface crust during drainout of the liquid core or active disruption of the crust due to high shear rates at the channel margins.

[47] 3. Numerical modeling of the flow of lava through idealized channels yields volume fluxes of $0.4–4.7 \times 10^3$ m³/s. Model estimates are confirmed by comparison to analog models that show similar surface morphology distributions. These flux values are lower than those inferred by previous analog and numerical studies, in part due to more accurate measurements of channel depths, widths, and slopes from high-resolution data sources.

[48] 4. Mapping and geochemical evidence indicate that channelized flows are erupted at the AST, despite the absence of surface channels within 50–300 m of AST for some channel systems. In those cases, we are able to determine that the channels have been covered by later flows or that evidence of the channels was destroyed by wholesale collapse of a AST-proximal inflated portion of the flow.

[49] 5. We find that high lava channel abundance can be correlated with variations in across axis morphology. The regions with the greatest number of channels have a rectangular axial cross section indicative of an increased magma budget. Whether the presence of channelized flows is responsible for the cross axis shape cannot be determined definitively, but the correlation between the channel abundance and ridge asymmetry would suggest that channelized flow emplacement has strongly influenced the morphology of the EPR in this area over the past ∼10 ka.

[50] 6. The high effusion rate and on axis source of the channels supports the conclusion that channelized flows are a primary mechanism for the 200–300% thickening of the extrusive layer (2A) within ∼2 km of the axis that has been observed at fast and superfast spreading ridges. This is shown to be true in the regions with the greatest channel abundance, and where layer 2A thickening is most dramatic.

[51] 7. Positive correlations exist between long-timescale (60 ka) features of the ridge crest, such as layer 2A geometry and ridge-crest morphology and asymmetry, and the presence of short timescale (10 ka) features, such as channelized flows. One possible explanation for this correlation is that volcanic accretion processes implied by short timescale channels are longer lived, and that some

portions of the EPR are more likely to have high volumetric flux eruptions that lead to channelized flows.

## Acknowledgments

## References

Adams, D. M. (2001), Cooling the young sheet flow on the Juan de Fuca Ridge, Masters thesis, Univ. at Buffalo, State Univ. of New York, Buffalo, N. Y.

Asimow, P. D., and M. S. Ghiorso (1998), Algorithmic modifications extending MELTS to calculate subsolidus phase relations, *Am. Mineral.*, *83*, 1127–1132.

Bach, W., S. E. Humphris, and A. T. Fisher (2004), Fluid flow and fluid-rock interaction within ocean crust: Reconciling geochemical, geological, and geophysical observations, in *The Subsurface Biosphere at Mid-Ocean Ridges*, *Geophys. Monogr. Ser.*, vol. 144, edited by W. S. D. Wilcock et al., pp. 99–118, AGU, Washington, D. C.

Ballard, R. D., and T. H. van Andel (1977), Morphology and tectonics of the inner rift valley at 36°50′N on the Mid-Atlantic Ridge, *Geol. Soc. Am. Bull.*, *88*, 507–530.

Ballard, R. D., W. B. Bryan, J. R. Heirtzler, G. Keller, J. G. Moore, and T. H. van Andel (1975), Manned submersible observations in the FAMOUS area: Mid-Atlantic Ridge, *Science*, *190*, 103–108.

Batchelor, G. K. (1967), *An Introduction to Fluid Dynamics*, 609 pp., Cambridge Univ. Press, New York.

Batiza, R., and S. H. Margolis (1986), Small non-overlapping offsets of the East Pacific Rise, *Nature*, *320*, 439–441.

Bellaiche, G., J. L. Cheminee, J. Francheteau, R. Hekinian, X. Le Pichon, H. D. Needham, and R. D. Ballard (1974), Inner floor of the Rift Valley: First submersible study, *Nature*, *250*, 558–560.

Bohnenstiehl, D. R., and M. C. Kleinrock (2000), Fissuring near the TAG active hydrothermal mound 26°N on the Mid-Atlantic Ridge, *J. Volcanol. Geotherm. Res.*, *98*, 33–48.

Bryan, W. B., S. E. Humphris, G. Thompson, and J. F. Casey (1994), Comparative volcanology of small axial eruptive centers in the MARK area, *J. Geophys. Res.*, *99*, 2973–2984.

Carbotte, S., and K. Macdonald (1992), East Pacific Rise 8°–10°30′N: Evolution of ridge segments and discontinuities from SeaMARC II and three-dimensional magnetic studies, *J. Geophys. Res.*, *97*, 6959–6982.

Carbotte, S. M., J. C. Mutter, and X. Liqing (1997), Contribution of volcanism and tectonism to axial flank morphology of the southern East Pacific Rise, 17°10′–17°40′S, from a study of 2A geometry, *J. Geophys. Res.*, *102*, 10,165–10,184.

Cashman, K. V., C. Thornber, and J. P. Kauahikaua (1999), Cooling and crystallization of lava in open channels, and the transition of pahoehoe lava to ′a′a, *Bull. Volcanol.*, *61*, 306–323.

Chadwick, W. W., Jr. (2003), Quantitative constraints on the growth of submarine lava pillars from a monitoring instrument that was caught in a lava flow, *J. Geophys. Res.*, *108*(B11), 2534, doi:10.1029/2003JB002422.

Chadwick, W. W., D. S. Scheirer, R. W. Embley, and H. P. Johnson (2001), High-resolution bathymetric surveys using scanning sonars: Lava flow morphology, hydrothermal vents, and geologic structure at recent eruption sites on the Juan de Fuca Ridge, *J. Geophys. Res.*, *106*, 16,075–16,099.

Christeson, G. L., G. M. Purdy, and G. J. Fryer (1992), Structure of young upper crust at the East Pacific Rise near 9°30′N, *Geophys. Res. Lett.*, *19*, 1045–1048.

Christeson, G. L., G. M. Purdy, and G. J. Fryer (1994a), Seismic constraints on shallow crustal emplacement processes at the fast-spreading East Pacific Rise, *J. Geophys. Res.*, *99*, 17,957–17,973.

Christeson, G. L., W. S. D. Wilcock, and G. M. Purdy (1994b), The shallow attenuation structure of the fast-spreading East Pacific Rise near 9°30′N, *Geophys. Res. Lett.*, *21*, 321–324.

Christeson, G. L., G. M. Kent, G. M. Purdy, and R. S. Detrick (1996), Extrusive thickness variability at the East Pacific Rise, 9°–10°N: Constraints from seismic techniques, *J. Geophys. Res.*, *101*, 2859–2873.

Cochran, J. R., D. J. Fornari, B. J. Coakley, R. Herr, and M. A. Tivey (1999), Continuous near-bottom gravity measurements made with a BGM-3 gravimeter is DSV *Alvin* on the East Pacific Rise crest near 9°30′N and 9°50′N, *J. Geophys. Res.*, *104*, 10,841–10,861.

Cormier, M. H., W. B. F. Ryan, A. K. Shah, W. Jin, A. M. Bradley, and D. R. Yoerger (2003), Waxing and waning volcanism along the East Pacific Rise on a millennium time scale, *Geology*, *31*, 633–636.

Crane, K., and R. D. Ballard (1981), Volcanics and structure of the FAMOUS Narrowgate rift: Evidence for cyclic evolution: AMAR 1, *J. Geophys. Res.*, *86*, 5112–5124.

Crawford, W. C., and S. C. Webb (2002), Variations in the distribution of magma in the lower crust and at the Moho beneath the East Pacific Rise at 9°–10°N, *Earth Planet. Sci. Lett.*, *203*, 117–130.

Delaney, J. R., D. S. Kelley, M. D. Lilley, D. A. Butterfield, J. A. Baross, W. S. D. Wilcock, R. W. Embley, and M. Summit (1998), The quantum event of oceanic crustal accretion: Impacts of diking at mid-ocean ridges, *Science*, *281*, 222–230.

Detrick, R. S., J. C. Mutter, P. Buhl, A. J. Harding, G. M. Kent, and J. A. Orcutt (1993), Seismic structure of the southern East Pacific Rise, *Science*, *259*, 499–503.

Edwards, K. J., T. M. McCollom, H. Konishi, and P. R. Buseck (2003), Seafloor bio-alteration of sulfide minerals: Results from in-situ incubation studies, *Geochim. Cosmochim. Acta*, *67*, 2843–2856.

Embley, R. W., and W. W. Chadwick (1994), Volcanic and hydrothermal processes associated with a recent phase of seafloor spreading at the northern Cleft Segment: Juan de Fuca Ridge, *J. Geophys. Res.*, *99*, 4741–4760.

Embley, R. W., W. W. Chadwick, M. R. Perfit, M. C. Smith, and J. R. Delaney (2000), Recent eruptions on the CoAxial segment of the Juan de Fuca Ridge: Implications for mid-

ocean ridge accretion process, *J. Geophys. Res.*, *105*(B7), 16,501–16,525.

Engels, J. L., M. H. Edwards, D. J. Fornari, M. R. Perfit, and J. R. Cann (2003), A new model for submarine volcanic collapse formation, *Geochem. Geophys. Geosyst.*, *4*(9), 1077, doi:10.1029/2002GC000483.

Ferrini, V. L., D. J. Fornari, T. M. Shank, M. A. Tivey, D. S. Kelley, D. Glickson, S. Carbotte, J. Howland, L. L. Whitcomb, and D. R. Yoerger (2004), Very high resolution bathymetric mapping at the Ridge2000 Integrated study sites: Acquisition and processing protocols developed, *Eos Trans. AGU*, *85*(47), Fall Meet. Suppl., Abstract B13A-0162.

Fink, J. H., and R. W. Griffiths (1990), Radial spreading of viscous-gravity currents with solidifying crust, *J. Fluid Mech.*, *221*, 485–509.

Fink, J. H., and R. W. Griffiths (1992), A laboratory analog study of the surface morphology of lava flows extruded from point and line sources, *J. Volcanol. Geotherm. Res.*, *54*, 19–32.

Fornari, D. J., M. H. Edwards, R. M. Haymon, M. R. Perfit, and T. K. P. Gregg (1998), Axial summit trough of the East Pacific Rise 9°–10°N: Geological characteristics and evolution of the axial zone on fast spreading mid-ocean ridges, *J. Geophys. Res.*, *103*, 9827–9855.

Fornari, D. J., et al. (2004), Submarine lava flow emplacement at the East Pacific Rise 9°50′N: Implications for uppermost ocean crust stratigraphy and hydrothermal fluid circulation, in *Mid-Ocean Ridges: Hydrothermal Interactions Between the Lithosphere and Oceans*, *Geophys. Monogr. Ser.*, vol. 148, edited by C. R. German, J. Lin, and L. M. Parson, pp. 187–218, AGU, Washington, D. C.

Fox, C. G., W. W. Chadwick, and R. W. Embley (2001), Direct observation of a submarine volcanic eruption from a seafloor instrument caught in a lava flow, *Nature*, *412*, 727–729.

Ghiorso, M. S., and R. O. Sack (1995), Chemical mass transfer in magmatic processes. IV. A revised and internally consistent thermodynamic model for the interpolation and extrapolation of liquid-solid equilibria in magmatic systems at elevated temperatures and pressures, *Contrib. Mineral. Petrol.*, *119*, 197–212.

Goldstein, S. J., M. R. Perfit, R. Batiza, D. J. Fornari, and M. T. Murrell (1994), Off-axis volcanism at the East Pacific Rise detected by uranium-series dating of basalts, *Nature*, *367*, 157–159.

Gregg, T. K., and W. W. Chadwick (1996), Submarine lava flow inflation: A model for the formation of lava pillars, *Geology*, *24*, 981–984.

Gregg, T. K., and J. H. Fink (1995), Quantification of submarine lava-flow morphology through analog experiments, *Geology*, *23*, 73–76.

Gregg, T. K. P., D. J. Fornari, M. R. Perfit, R. M. Haymon, and J. H. Fink (1996), Rapid emplacement of a mid-ocean ridge lava flow on the East Pacific Rise at 9°46′–51′N, *Earth Planet. Sci. Lett.*, *144*, E1–E7.

Gregg, T. K., D. J. Fornari, M. R. Perfit, W. I. Ridley, and M. D. Kurz (2000), Using submarine lava pillars to record mid-ocean ridge eruption dynamics, *Earth Planet. Sci. Lett.*, *178*, 195–214.

Griffiths, R. W., and J. H. Fink (1992), The morphology of lava flows in planetary environments: Predictions from analog experiments, *J. Geophys. Res.*, *97*, 19,739–19,748.

Griffiths, R. W., R. C. Kerr, and K. V. Cashman (2003), Patterns of solidification in channel flows with surface cooling, *J. Fluid Mech.*, *496*, 33–62.

Harding, A. J., G. M. Kent, and J. A. Orcutt (1993), A multichannel seismic investigation of upper crustal structure at 9°N on the East Pacific Rise: Implications for crustal accretion, *J. Geophys. Res.*, *98*, 13,925–13,944.

Haymon, R. M., D. J. Fornari, M. H. Edwards, S. M. Carbotte, D. Wright, and K. C. Macdonald (1991), Hydrothermal vent distribution along the East Pacific Rise crest (9°9′–54′N) and its relationship to magmatic and tectonic processes on fast-spreading mid-ocean ridges, *Earth Planet. Sci. Lett.*, *104*, 513–534.

Haymon, R. M., et al. (1993), Volcanic eruption of the mid-ocean ridge along the East Pacific Rise crest at 9°45–52′N: Direct submersible observations of seafloor phenomena associated with an eruption event in April, 1991, *Earth Planet. Sci. Lett.*, *119*, 85–101.

Heliker, C., and T. N. Mattox (2003), The first two decades of the Pu'u 'O'o-Kupaianaha eruption: Chronology and selected bibliography, in *The Pu'u 'O'o-Kupaianaha Eruption of Kilauea Volcano, Hawai'i: The First 20 Years*, edited by C. Heliker, D. A. Swanson, and T. J. Takahashi, U.S. Geol. Surv., Reston, Va.

Hooft, E. E., H. Schouten, and R. S. Detrick (1996), Constraining crustal emplacement processes from the variation in seismic layer 2A thickness at the East Pacific Rise, *Earth Planet. Sci. Lett.*, *142*, 289–309.

Kent, G. M., J. C. Mutter, P. Buhl, A. J. Harding, J. A. Orcutt, and R. S. Detrick (1994), Uniform accretion of oceanic crust south of the Garrett transform at 14°15′S on the East Pacific Rise, *J. Geophys. Res.*, *99*, 9097–9116.

Kilburn, C. R. J. (1990), Surfaces of aa flow-fields on Mount Etna, Sicily: Morphology, rheology, crystallization and scaling phenomena, in *Lava Flows and Domes: Emplacement Mechanisms and Hazard Implications*, edited by J. H. Fink, pp. 129–156, Springer, New York.

Knudsen, J. G., and D. L. Katz (1958), *Fluid Dynamics and Heat Transfer*, 349 pp., McGraw-Hill, New York.

Kurras, G. J., M. C. Smith, D. J. Fornari, M. H. Edwards, and M. R. Perfit (2000), Volcanic morphology of the East Pacific Rise Crest 9°49′–52′: Implications for volcanic emplacement processes at fast-spreading mid-ocean ridges, *Mar. Geophys. Res.*, *21*, 23–41.

Landau, L., and E. Lifschitz (1971), *Mechanique des Fluides*, 670 pp., MIR, Moscow.

Langmuir, C. H., J. F. Bender, and R. Batiza (1986), Petrological and tectonic segmentation of the East Pacific Rise, 5°30′–14°30′N, *Nature*, *322*, 422–429.

Langmuir, C. H., E. M. Klein, and T. Plank (1992), Petrological systematics of mid-ocean ridge basalts: Constraints on melt generation beneath ocean ridges, in *Mantle Flow and Melt Generation at Mid-Ocean Ridges*, *Geophys. Monogr. Ser.*, vol. 71, edited by J. Phipps Morgan, D. K. Blackman, and J. M. Sinton, pp. 183–280, AGU, Washington, D. C.

Lockwood, J. P., J. J. Dvorak, T. T. English, R. Y. Koyanagi, A. T. Okamura, M. L. Summers, and W. R. Tanigawa (1987), Mauna Loa 1974–1984: A decade of intrusive and extrusive activity, *U.S. Geol. Surv. Prof. Pap.*, *1350*, 537–570.

Macdonald, K. C., and P. J. Fox (1988), The axial summit graben and cross-sectional shape of the East Pacific Rise as indicators of axial magma chambers and recent volcanic eruptions, *Earth Planet. Sci. Lett.*, *88*, 119–131.

Macdonald, K., J.-C. Sempere, and P. J. Fox (1984), East Pacific Rise from Siqueiros to Orozco fracture zones: Along-strike continuity of axial neovolcanic zone and structure and evolution of overlapping spreading centers, *J. Geophys. Res.*, *89*, 6049–6069.

Macdonald, K. C., et al. (1992), The East Pacific Rise and its flanks 8–18°: History of segmentation, propagation and spreading direction based on SeaMARC II and Sea Beam studies, *Mar. Geophys. Res.*, *14*, 299–344.

Mayer, L., Y. Rzhanov, D. J. Fornari, A. Soule, T. M. Shank, S. E. Beaulieu, H. Schouten, and M. A. Tivey (2004), Mosaicking techniques for deep submergence vehicle video imagery: Applications to Ridge2000 science, *Eos Trans. AGU*, *85*(47), Fall Meet. Suppl., Abstract B13A-0162.

Perfit, M. R., and W. W. Chadwick (1998), Magmatism at mid-ocean ridges: Constraints from volcanological and geochemical investigations, in *Faulting and Magmatism at Mid-Ocean Ridges*, *Geophys. Monogr. Ser.*, vol., edited by W. R. Buck et al., pp. 59–116, AGU, Washington, D. C.

Perfit, M. R., D. J. Fornari, M. C. Smith, J. F. Bender, C. H. Langmuir, R. M. Haymon, and J. F. Bender (1994), Small scale spatial and temporal variations in mid-ocean ridge crest magmatic processes, *Geology*, *22*, 375–379.

Perfit, M. R., J. R. Cann, D. J. Fornari, J. Engels, D. K. Smith, W. I. Ridley, and M. H. Edwards (2003), Interaction of sea water and lava during submarine eruptions at mid-ocean ridges, *Nature*, *426*, 62–65.

Phillpotts, A. R. (1990), *Principles of Igneous and Metamorphic Petrology*, Prentice-Hall, Upper Saddle River, N. J.

Reynolds, J. R., and C. H. Langmuir (2000), Identification and implications of off-axis lava flows around the East Pacific Rise, *Geochem. Geophys. Geosyst.*, *1*(6), doi:10.1029/1999GC000033.

Reynolds, J. R., C. H. Langmuir, J. F. Bender, K. A. Kastens, and W. B. F. Ryan (1992), Spatial and temporal variability in the geochemistry of basalts from the East Pacific Rise, *Nature*, *359*, 493–499.

Rubin, K. H., M. R. Perfit, J. M. Sinton, R. Batiza, M. C. Smith, and E. C. Bergmanis (2001), Geochemical heterogeneity within mid-ocean ridge lava flows: Insights into eruption, emplacement and global variations in magma generation, *Earth Planet. Sci. Lett.*, *188*(3–4), 349–367.

Ryan, W. B. F., M.-H. Cormier, A. M. Bradley, D. R. Yoerger, and H. Singh (1999), Branching and confluence of axially-fed lava channels on the crest of the East Pacific Rise at 17°28′S, *Eos Trans. AGU*, *80*(46), Fall Meet. Suppl., Abstract V11A-14.

Sakimoto, S. E. H., and T. K. P. Gregg (2001), Channeled flow: Analytic solutions, laboratory experiments, and applications to lava flows, *J. Geophys. Res.*, *106*, 8629–8644.

Scheirer, D. S., and K. C. Macdonald (1993), Variation in cross-sectional area of the axial ridge along the East Pacific Rise: Evidence for the magmatic budget of a fast-spreading center, *J. Geophys. Res.*, *98*, 7871–7885.

Scheirer, D. S., D. J. Fornari, S. E. Humphris, and S. Lerner (2000), High-resolution seafloor mapping using the DSL-120 sonar system: Quantitative assessment of sidescan and phase-bathymetry data from the Lucky Strike segment of the mid-Atlantic ridge, *Mar. Geophys. Res.*, *21*, 121–142.

Schouten, H., M. A. Tivey, D. J. Fornari, and J. R. Cochran (1999), Central anomaly magnetization high: Constraints on the volcanic construction and architecture of seismic layer 2A at a fast spreading mid-ocean ridge, *Earth Planet. Sci. Lett.*, *169*, 37–50.

Schouten, H., M. A. Tivey, D. J. Fornari, D. R. Yoerger, A. M. Bradley, P. Johnson, M. H. Edwards, and T. Kurokawa (2002), Lava transport and accumulation processes on EPR 9°27′N to 10°N: Interpretations based on recent near-bottom sonar imaging and seafloor observations using ABE, *Alvin*, and a new digital deep sea camera, *Eos Trans. AGU*, *83*(47), Fall Meet. Suppl., Abstract T11C-1262.

Shank, T. M., D. J. Fornari, K. L. Von Damm, M. D. Lilley, R. M. Haymon, and R. A. Lutz (1998), Temporal and spatial patterns of biological community development at nascent deep-sea hydrothermal vents along the East Pacific Rise, *Deep Sea Res., Part II*, *45*, 465–515.

Sims, K. W. W., et al. (2003), Aberrant youth: Chemical and isotopic constraints on the origin of off-axis lavas from the East Pacific Rise, 9°–10°N, *Geochem. Geophys. Geosyst.*, *4*(10), 8621, doi:10.1029/2002GC000443.

Sinton, J., E. Bergmanis, K. Rubin, R. Batiza, T. K. P. Gregg, K. Grönvold, K. C. Macdonald, and S. M. White (2002), Volcanic eruptions on mid-ocean ridges: New evidence from the superfast spreading East Pacific Rise, 17°–19°S, *J. Geophys. Res.*, *107*(B6), 2115, doi:10.1029/2000JB000090.

Smith, D. K., and J. R. Cann (1990), Hundreds of small volcanoes on the median valley floor of the Mid- Atlantic Ridge at 24–30°N, *Nature*, *348*, 152–155.

Smith, M. C., M. R. Perfit, D. J. Fornari, W. I. Ridley, M. H. Edwards, G. J. Kurras, and K. L. Von Damm (2001), Magmatic processes and segmentation at a fast spreading mid-ocean ridge: Detailed investigation of an axial discontinuity on the East Pacific Rise crest at 9°37′, *Geochem. Geophys. Geosyst.*, *2*(10), doi:10.1029/2000GC000134.

Sohn, R. A., S. C. Webb, and J. A. Hildebrand (2004), Fine-scale seismic structure of the shallow volcanic crust on the East Pacific Rise at 9°50′N, *J. Geophys. Res.*, *109*, B12104, doi:10.1029/2004JB003152.

Soule, S. A., and K. V. Cashman (2004), The mechanical properties of solidified polyethylene glycol 600, an analog for lava crust, *J. Volcanol. Geotherm. Res.*, *129*, 139–153.

Soule, S. A., and K. V. Cashman (2005), Shear rate dependence of the pahoehoe to ′a′a transition, *Geology*, *33*(5), 361–364, doi:10.1130/G21269.1.

Soule, S. A., K. V. Cashman, and J. P. Kauahikaua (2004), Examining flow emplacement through the surface morphology of three rapidly emplaced, solidified lava flows, Kilauea Volcano, Hawaii, *Bull. Volcanol.*, *66*, 1–14.

Spera, F. J. (2000), Physical properties of magma, in *Encyclopedia of Volcanoes*, edited by H. Sigurdsson, pp. 171–190, Elsevier, New York.

Tallarico, A., and M. Dragoni (1999), Viscous Newtonian laminar flow in a rectangular channel: Application to Etna lava flows, *Bull. Volcanol.*, *61*, 40–47.

Thordarsson, T., and S. Self (1993), The Laki (Skaftar Fires) and Grimsvotn eruptions in 1783–1785, *Bull. Volcanol.*, *55*, 233–263.

Timoshenko, S., and J. N. Goodier (1951), *Theory of Elasticity*, McGraw-Hill, New York.

Vera, E. E., and J. B. Diebold (1994), Seismic imaging of oceanic layer 2A between 9°30′N and 10°N on the East Pacific Rise from two-ship wide-aperture profiles, *J. Geophys. Res.*, *99*, 3031–3041.

Von Damm, K. L., L. G. Buttermore, S. E. Oosting, A. M. Bray, D. J. Fornari, M. D. Lilley, and W. C. Shanks (1997), Direct observation of the evolution of a seafloor "black smoker" from vapor to brine, *Earth Planet. Sci. Lett.*, *149*, 101–111.

White, S. M., R. M. Haymon, D. J. Fornari, M. R. Perfit, and K. C. Macdonald (2002), Correlation between volcanic and tectonic segmentation of fast-spreading ridges: Evidence from volcanic structures and lava flow morphology on the East Pacific Rise at 9°–10°N, *J. Geophys. Res.*, *107*(B8), 2173, doi:10.1029/2001JB000571.

Williams, H., and A. R. McBirney (1979), *Volcanology*, W. H. Freeman, New York.

Wolfe, E. W., C. A. Neal, N. G. Banks, and T. J. Duggan (1988), Geologic observations and chronology of eruptive events, in *The Puu Oo Eruption of Kilauea Volcano, Hawaii: Episodes 1 Through 20, January 3, 1983, Through June 8, 1984*, edited by E. W. Wolfe, pp. 1–98, U.S. Geol. Surv., Reston, Va.